



# Characteristics of hail hazard in South Africa based on satellite detection of convective storms

Heinz Jürgen Punge<sup>1</sup>, Kristopher M. Bedka<sup>2</sup>, Michael Kunz<sup>1</sup>, Sarah D. Bang<sup>3</sup>, and Kyle F. Itterly<sup>4</sup>

<sup>1</sup>Institute of Meteorology and Climate Research, Karlsruhe Institute of Technology (KIT), Karlsruhe, Germany

<sup>2</sup>NASA Langley Research Center, Science Directorate, Climate Science Branch, Hampton, VA, USA

<sup>3</sup>NASA Marshall Space Flight Center (ST-11), Huntsville, AL, USA

<sup>4</sup>Science Systems and Applications Inc., Hampton, VA, USA

**Correspondence:** Michael Kunz ([michael.kunz@kit.edu](mailto:michael.kunz@kit.edu))

Received: 12 November 2021 – Discussion started: 25 November 2021

Revised: 10 March 2023 – Accepted: 20 March 2023 – Published: 26 April 2023

**Abstract.** Accurate estimates of hail risk to exposed assets, such as crops, infrastructure, and vehicles, are required for both insurance pricing and preventive measures. Here we present an event catalog to describe the hail hazard in South Africa guided by 14 years of geostationary satellite observations of convective storms. Overshooting cloud tops have been detected, grouped, and tracked to describe the spatiotemporal extent of potential hail events. It is found that hail events concentrate mainly in the southeast of the country, along the Highveld, and around the eastern slopes. Events are most frequent from mid-November through February and peak in the afternoon, between 13:00 and 17:00 UTC. Multivariate stochastic modeling of event properties yields an event catalog spanning 25 000 years, aiming to estimate, in combination with vulnerability and exposure data, hail risk for return periods of 200 years.

## 1 Introduction

Damage from large hail is a significant contribution to natural hazard losses in many parts of the world (Punge and Kunz, 2016; Púčik et al., 2019; Allen et al., 2020), including South Africa, and growing research activity has opened up opportunities to estimate risk for the insurance sector (Punge et al., 2014; Rädler et al., 2023). In South Africa, hail has long been known to generate large amounts of damage to agriculture – around 2 % of the value of products (Carte, 1977) – and forestry (Smith et al., 2002; Wingfield and Swart, 1994). Events with severe hail damage to buildings, vehi-

cles, and infrastructure like the one on 28 November 2013 (total loss ZAR 1.4 billion, around USD 140 million, Powell and Burger, 2014) are numerous (e.g., Perry, 1995). Still, in comparison to other natural hazards, the sporadic occurrence and highly localized effects of hail pose a particular challenge to hazard quantification, which forms the basis for any risk modeling. Such modeling is required for the insurance sector to estimate the financial risks related to a hazard, as required, for example, by the Insurance Act 18 of 2017, and can guide measures to improve resilience.

Across the world, reliable records of hailfall including size information are limited to reports by volunteer observer networks (e.g., Held, 1974) and other sources, sometimes collected in databases of hail reports (e.g., Dotzek et al., 2009; Allen et al., 2015) or hailpad networks (e.g., Palencia et al., 2009). Leigh and Kuhnel (2001), for example, constructed a regional risk model based on such reports and loss data alone. Grieser and Hill (2019) used volunteer-collected hail observations in the United States (Reges et al., 2016) to model the rate of hailstones hitting the ground per unit area, time, and hailstone size bin during the passage of a hailstorm. Based on that data, they set up a model to calculate the vulnerability of subjects at risk as a function of the diameter of the largest hailstone, which can be transferred to other regions.

For South Africa, Admirat et al. (1985) evaluated hailpad and hail reports from a network of voluntary hail observers (mainly farmers equipped with hail cards) to quantify hail properties in an area of 280 km<sup>2</sup> in the Transvaal Highveld (HVD), nowadays a part of the Gauteng region (see Fig. 2a). Using reports from the same network over a 19-year period,

Smith et al. (1998) found on average 68.5 hail days per year, much more than in other regions of similar size, for example, northern Italy, which is the highest hail-exposed region in Europe (e.g., Giaioiti et al., 2003; Punge et al., 2017). Of these, 3.3 d had hail greater than 3 cm.

While distinction between hail and rain or sleet is often challenging, remote sensing data from either radar or satellite instruments are required to determine the spatial extent of hail events and to depict the geographic distribution of the hazard (Puskeiler et al., 2016; Bedka et al., 2017; Nisi et al., 2018; Allen et al., 2020). Alternatively, numerical models such as high-resolution reanalysis can be used to identify atmospheric conditions favorable for hailstorm formation (e.g., Rädler et al., 2023; Kunz et al., 2020; Taszarek et al., 2020). In that case, climatologies over long time series can be generated (Dyson et al., 2020; Prein and Holland, 2018). These are, however, generally limited by model resolution and the inaccurate representation of convective initiation, since hailstorms often form by local-scale and mesoscale processes related to, for example, orographic lifting and mountain winds, low-level convergence zones, or land use inhomogeneities (Allen et al., 2020). In addition, reanalyses or regional climate models use simplified microphysical parameterization schemes and not two- or even three-moment schemes required for more realistic hail size modeling (Seifert and Beheng, 2006; Loftus et al., 2014; Wellmann et al., 2020). Several studies have used hail signals or hail detection algorithms for hail frequency assessments (Cintineo et al., 2012; Junghänel et al., 2016; Fluck et al., 2021) and risk modeling (Puskeiler et al., 2016; Nisi et al., 2018; Schmidberger, 2018). However, radar data are usually only available on country scales due to availability and inter-radar calibration issues. In South Africa, the use of radar data for nowcasting of hail has been studied for the Highveld region (Ayob, 2019). However, the South African radar network does not cover the entire country.

Even though satellite data are a less accurate proxy for hailstorm detection compared to radar, the big advantage is that these data cover comparatively larger areas almost homogeneously. The detection of hail via scattering of upwelling Earth-emitted microwave radiation is currently limited to satellites in low-earth orbit (Mroz et al., 2017; Ni et al., 2017; Bang and Cecil, 2019). Such data can be exploited for global analysis of hail occurrence as well as for identification of atmospheric conditions prevailing during individual hailstorms. The drawback, however, is the lack of temporal coverage required to examine the evolution of hailstorms. In contrast, indirect indicators have been designed to extract severe weather and hail signals from much more frequent and spatially detailed geostationary satellite imagery (Bedka et al., 2010; Melcón et al., 2016).

An overshooting cloud top (OT) indicates an intense updraft capable of generating hail. The OTs can be detected in both visible and infrared data (Bedka and Khlopenkov, 2016; Khlopenkov et al., 2021). In particular, the most severe hail-

storms show a clear OT signature (e.g., Kunz et al., 2018; Wilhelm et al., 2021). The OT detection algorithm has been extensively calibrated and tested against severe weather reports and radar data (Bedka and Khlopenkov, 2016; Sandmæl et al., 2019; Cooney et al., 2021). Still, in some cases, OT features may have been misdetected or may not have produced hail on the ground, for example, due to melting of hailstones during fall through a deep column of warm air. This is acknowledged in the studies of Punge et al. (2014, 2017) and by Bedka et al. (2018a), who noted the large percentages of OTs without hail on the ground. However, in addition to the hazard modeling purpose, the focus of our study is on the identification of larger spatial severe convective storm (SCS) clusters with an increased potential of hail production during the lifetime of the event, rather than detecting each individual storm with enhanced hail potential. These large-scale hail-producing outbreaks can cause by far the largest part of the damage registered by insurers and can induce solvency issues when the risk is not properly estimated.

Punge et al. (2014, 2017) used the OT approach to estimate a hail event dataset for Europe which served as the physical basis for the Willis European Hail Model, the first fully randomized stochastic hail model to cover all of Europe. Since 2014, the model has been established as a standard tool in hail risk estimation and pricing among insurance and reinsurance companies in Europe. A similar approach was later applied to Australia (Bedka et al., 2018b). However, assessments of this kind are absent in many emerging insurance companies and markets around the world. Of these, South Africa is a prime example of where hail is a common hazard and major risk driver. Therefore, we focus on South Africa in this article, refining the methodology of Punge et al. (2014, 2017) to describe hail events more accurately. In contrast to Bedka et al. (2010), the Khlopenkov et al. (2021) OT detection technique, which was applied here, provided a gridded probabilistic representation of an OT rather than a list of OT centroid pixel locations, accounting for both size and reliability of the updraft detections. The event definition procedure now tracks storm signatures over time, allowing us to follow convective activity more closely. In the stochastic component of the model, rather than simply re-sampling historic events to describe possible future hazards, distributions of relevant event properties are modeled and sampled separately, conserving correlation among these properties. Improvements compared to the European and Australian hail models concern event definition, event parameter distributions, and detail of the stochastically generated footprints.

Section 2 presents the methodology and datasets used as input for the model, whereas Sect. 3 describes the derived hazard distribution and OT event sets. Stochastic event sampling and potential hail footprint generation are discussed in Sect. 4.

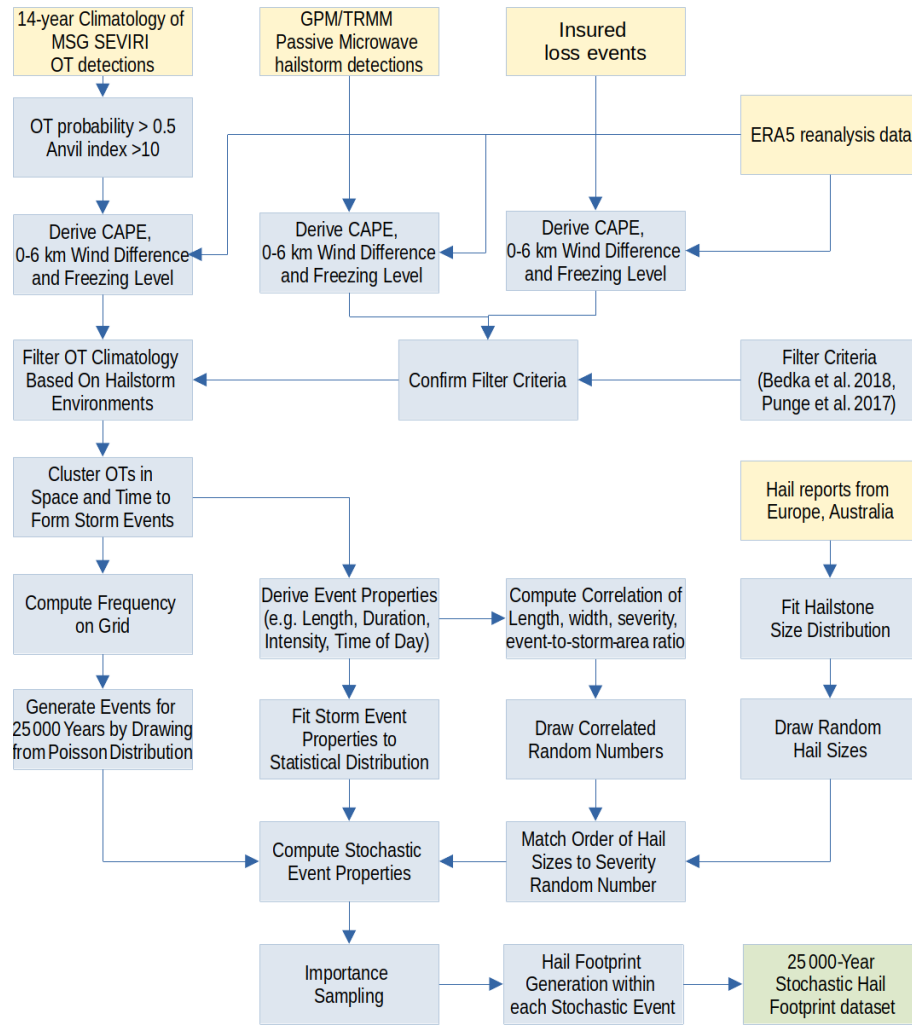


Figure 1. Diagram illustrating the functioning of the hail hazard model for South Africa.

2 Methods and data

The diagram in Fig. 1 illustrates how the different data sources, explained in the following, are combined in the model and processed to yield a set of event footprints representing 25 000 years of hail-generating convective storms based on the climate and weather of the period 2005–2018. Important steps in the development of the final stochastic modeling are (i) filtering of OTs that are unreliable or unlikely to produce severe hail using both passive microwave hailstorm detections and insurance loss data combined with convective environments (convective available potential energy (CAPE), wind shear, melting level) from ERA5 reanalysis; (ii) clustering of OTs in space and time to attain single events; (iii) quantifying histograms of the most important event properties (length, width, duration, time of day, day of year) and their relations; (iv) considering a hailstone size spectrum from severe weather reports outside of the study area; (v) adjusting appropriate statistical distribution func-

tions to the different properties; (vi) stochastically generating (artificial) events that resemble the climatology of potential hail events and their characteristics; (vii) applying importance sampling to reduce the number of events; and, finally, (viii) computing single hail footprints for the stochastic event set. All the steps and procedures mentioned above will be explained in the following sections.

2.1 Study area

South Africa’s topography consists of a large central plateau with extensive grasslands; a continuous escarpment of mountain ranges surrounding the plateau on the west, south, and east; and a narrow strip of low-lying land near the coastline. The central plateau is bounded by the Great Escarpment (see Fig. 2a), a major topographical feature in Africa consisting of steep slopes that drop from the high central plateau toward the oceans that surround southern Africa on three sides. The eastern part of the Great Escarpment in the border region of

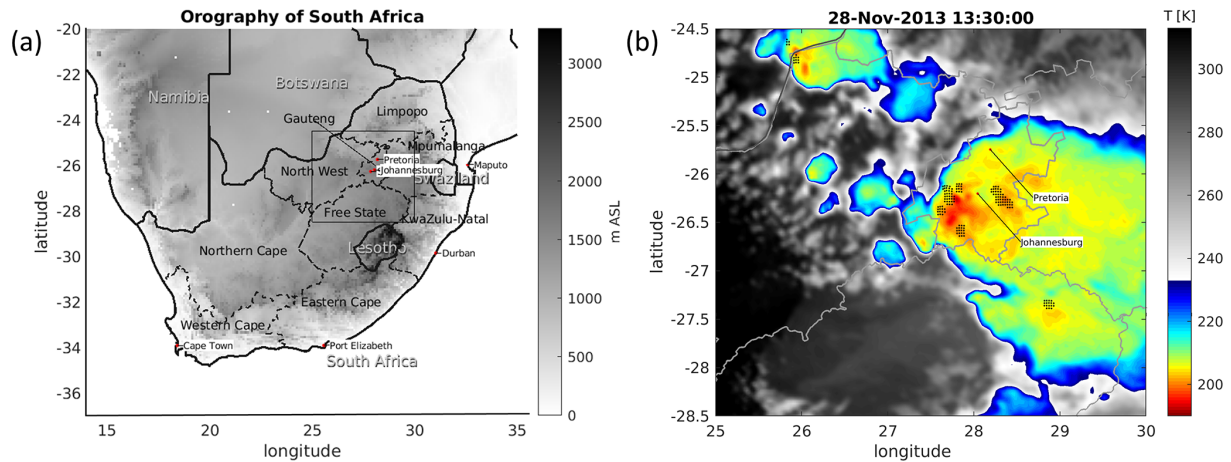


**Figure 2.** (a) Map showing the relief of South Africa from the Shuttle Radar Topography Mission (Farr et al., 2007), provinces, and major cities. Port Elizabeth and Swaziland are now Gqeberha and Eswatini, respectively. (b) Meteosat IR image showing convective storm activity on 28 November 2013 at 13:30 UTC. Colors represent  $10.8\ \mu\text{m}$  channel brightness temperature, and dots indicate detected overshooting tops (OTs, black) for this image. OT detections are parallax-corrected here but the underlying IR satellite image is not, leading to some slight displacement of a detection and a corresponding cold region. The anvil cloud in yellow and green colors is automatically detected using the IR anvil detection index greater than 10.

South Africa and Lesotho is the Drakensberg Escarpment. It is the highest mountain range in southern Africa, reaching an elevation of 3482 a.m.s.l. (above mean sea level).

South Africa's climate is determined by the subtropical zone of the Southern Hemisphere, the location between the Atlantic and the Indian oceans, and its orographic characteristics. Climate conditions, influenced by the ocean along the east and west coasts and the interior plateaus, vary between subtropical and temperate: subtropical in the northeast, Mediterranean in the southwest, and a warm dry desert environment in the central west and northwest.

## 2.2 Overshooting top detection

Intense thunderstorms are routinely observed by visible and infrared imagery from geostationary satellites for forecasting and warning purposes (Zinner et al., 2013; de Coning et al., 2015). In particular in the infrared channel, deep convective cloud tops atop updrafts appear as cold spots growing near to or above the tropopause level, surrounded by a warmer anvil (Adler et al., 1985). Cloudy air masses are propelled upwards in the storm's core before rebounding or dissolving again on timescales of a few minutes.

Detection of these OTs hereinafter referred to as OT detections has been automated by Bedka et al. (2010), revealing the climatological distribution in North America as well as in Europe (Bedka, 2011) and Australia (Bedka et al., 2018b). An advanced version of the OT detection algorithm described by Khlopenkov et al. (2021) delivers a 3 km gridded probabilistic estimate of OT likelihood based on a statistical combination of tropopause-relative infrared (IR) brightness temperature, prominence of an OT relative to the sur-

rounding anvil, and the area and spatial uniformity of the anvil cloud surrounding an OT candidate region. OTs detected with a probability  $> 50\%$  and with a surrounding anvil cloud (green and yellow colors in Fig. 2b) are used in this work (Scarino et al., 2020; Khlopenkov et al., 2021). The method was validated by Cooney et al. (2021) using OT identifications from gridded weather radar observations and by Khlopenkov et al. (2021) using human OT identifications over the United States (US). A relation between hail size estimated from radar and OT intensity has been suggested in several studies (e.g., Bedka, 2011).

In the Khlopenkov et al. (2021) study, the human analysts identified OTs with two confidence levels, resulting in a conservative mask with only the most confident OTs and a liberal mask that also included less confident OT identifications that did not appear as prominently in the imagery as those in the conservative mask. For the Geostationary Operational Environmental Satellite GOES-16, probability of detection (POD) at an OT probability  $> 0.5$  ranged from 0.51 to 0.95 and false alarm ratio (FAR) ranged from 0.04 to 0.24, with the highest POD for the conservative mask and the lowest FAR for the liberal mask. For GOES-13, POD decreased to 0.8 for the conservative mask but remained nearly the same as GOES-16 for the liberal mask. FAR increased by 0.10 for the liberal mask. In Cooney et al. (2021), an OT probability of 0.5 corresponded to a median 20 dBZ precipitation echo top near the tropopause and a FAR ranging from  $\sim 0.1$  to 0.5 depending on the reflectivity level used to define the precipitation echo top (e.g., 10 or 20 dBZ), the height of the echo, and the satellite data used as input (e.g., GOES-13 vs. GOES-16). POD based on these comparisons with echo tops ranged from 0.35 to 0.75. In summary, even the most prominent

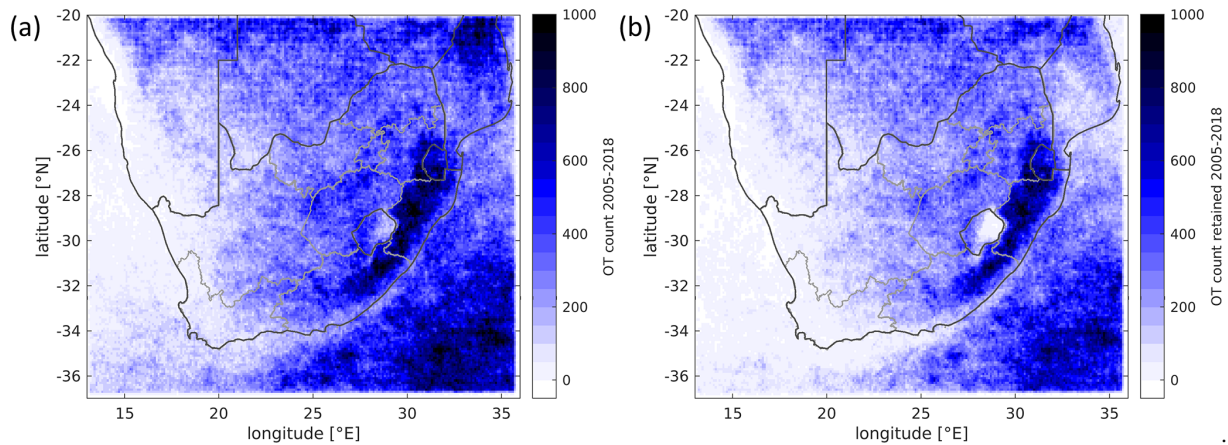


**Figure 3.** Map of (a) all OT pixel detections in the period 2005–2018 over continental South Africa and neighboring nations and seas (11 143 479 OTs) and (b) OT pixels retained after filtering for atmospheric conditions (8 272 509 OTs; see discussion in Sect. 2.6)

OTs are less evident and harder to detect in the GOES-13 data. Given the reduced prominence from coarser resolution, OT detection algorithm sensitivity settings must allow detection of smaller temperature gradients within anvils, which results in increased FAR.

False OT detections in very cold outflow near to actual OT regions is the most common source of error. Despite these false alarms, which in our opinion are impossible to completely eliminate, the Khlopenkov et al. (2021) OT detection method improves upon the Bedka et al. (2010) version used in previous hailstorm climatology studies and will represent the convection climatology across South Africa quite well.

Imagery of the Meteosat Second Generation (MSG) Spinning Enhanced Visible and Infrared Imager (SEVIRI) instrument (Schmetz et al., 2002) between January 2005 and December 2018 is scanned for OTs at a temporal resolution of 15 min. Since South Africa is not continuously covered by the high-resolution visible imagery product of MSG, only the IR channel data (given as  $10.8\ \mu\text{m}$  brightness temperature) are provided to the detection algorithm. An example is shown in Fig. 2b, where brightness temperature during a very strong hail event on 28 November 2013 and detected OTs are displayed.

The spatial distribution of OT pixel detections across the entire study domain and 14-year study duration is depicted in Fig. 3a. Clearly, convective storms are most common in the prevailing moist subtropical climate in east South Africa, along the Great Escarpment, including the southeastern flanks of the Drakensberg and stretching north through the Mpumalanga province (see Fig. 2a and Sect. 2.1). Here the complex terrain with a height of more than 2300 m a.s.l. induces uplift to serve as a trigger for convection initiation. By contrast, OT frequency decreases towards the west and towards the coast of the Indian Ocean, where the climate is mainly semi-arid to desert.

Compared to Dyson et al. (2020), we note the absence of an OT frequency maximum over the country of Lesotho, even in the unfiltered OT data, and higher values to the north and southeast. We attribute these differences to the coarse spatial resolution of the ERA-Interim reanalysis used in the above-mentioned study, which is likely insufficient to resolve local orography. The high altitudes in southern Lesotho (mostly 2500–3500 m a.s.l.; see Fig. 2a) seem to suppress deep convection to some degree, similar to the situation in the interior of the Alps in Europe (Punge and Kunz, 2016; Nisi et al., 2018).

### 2.3 Hail reports and insurance claims

Reports of hail observations including estimates of hail sizes are registered in several continental-scale, centralized databases for North America, Europe, and Australia. These reports are very helpful for validating the severity of the storms with detected OTs. In addition, derived hail size spectra are required as a measure of intensity in hail risk models. For South Africa no such database of comparable extent is available. However, comparing studies that estimated hail size spectra (e.g., Sánchez et al., 2009; Eccel et al., 2012; Dessens et al., 2015; Grieser and Hill, 2019), one can conclude that hail size spectra do not tend to vary greatly among regions and even continents. For this reason, we computed hail size spectra for the stochastic modeling component of this work from 26 884 hail reports archived by the European Severe Weather Database (ESWD; Dotzek et al., 2009) for the period 2005–2019 and from 3764 reports provided by the Severe Storms Archive of Australia’s Bureau of Meteorology for the period 1950–2019. Reporting policies meant that events of a hail diameter of 2 cm or more are covered, but in some cases reports with smaller stones accumulating to thick layers are included. A uniformly distributed random value between  $-0.5$  and  $+0.5$  cm was added to each reported hail

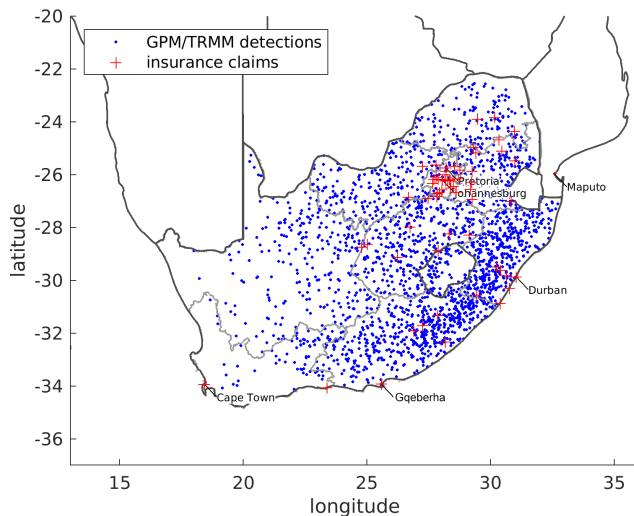


**Figure 4.** Claims locations of hail damage in South Africa (1984–2017) and passive microwave detections (1998–2018) in the model domain.

diameter to compensate for rounding in the hailstone measurement process and to obtain a smooth distribution.

In addition, 1423 hail damage claims between 1984 and 2017 including a reference to a location were obtained from several insurance companies of South Africa (see Fig. 4). Data did not include information on the size of hail, hour of occurrence, or type of asset affected. Claims data tend to be biased towards population centers and – in this case – towards major hail days but still has the advantage of providing direct evidence for hail occurrences.

#### 2.4 ERA5 reanalysis data

ERA5 (Hersbach et al., 2020) is the fifth-generation reanalysis of the European Centre for Medium-Range Weather Forecasts (ECMWF). It is a global observation-guided model representation of past weather. Data were obtained for the period 2005–2018 at a spatial resolution of  $0.25^\circ$  and hourly resolution. While CAPE and the height of the freezing level are provided as output variables, bulk wind difference between the near surface (10 m) and 6 km above the ground (0–6 km wind difference) was computed based on pressure-level data using linear interpolation.

#### 2.5 Passive microwave hail retrievals

Scattering of surface-emitted microwave radiation by hailstones is an alternative method of hailstorm detection by satellites (Cecil, 2009). The measurement principle has the advantage that in contrast to OTs the signal is directly caused by hailstones but at the cost of spatial and temporal coverage, commonly limited to two overpasses per day, and at the risk of nonuniform beam filling of the field of view. Beam sizes of current-generation sensors (e.g., Petty and Bennartz,

2017) are of the same order of magnitude as convective storm core diameters, meaning that the sensor and storm need to be aligned for successful detection.

In this work, such detections from the Tropical Rainfall Measuring Mission (TRMM) and the Global Precipitation Measurement Mission (GPM) satellites (Bang and Cecil, 2019, 2021) over the South African domain were evaluated for the period 1998–2019. Cases with a hail probability greater than 10 % over South Africa and Lesotho were retained. The threshold here is lower than in the studies cited above (threshold of 20 %) because our intention is to consider also small hail diameters and not just significant hail. Along with the damage claims, they are used to compare hail-prone environments in South Africa to those in Europe and Australia (Punge and Kunz, 2016; Bedka et al., 2018b) and to constrain OT detections to a certain range of convection-related parameters from ERA5 reanalysis (see next section).

#### 2.6 OT filtering by conditions from reanalysis

Before clustering the OT detections, a filter is applied based on surrounding atmospheric conditions in terms of wind shear and CAPE obtained from ERA5 for days and locations with microwave hail detections and damage reports (Fig. 5). Since insurance data are only available for South Africa (see Fig. 4), the filter criteria are also only determined for the territory of South Africa and Lesotho. Note that the purpose of this filter is distinct from other studies aiming to identify hail-prone conditions from reanalysis (e.g., Taszarek et al., 2020; Dowdy et al., 2020; Prein and Holland, 2018), which tend to suggest much stricter criteria.

The filter design used for Europe (Punge et al., 2017) and Australia (Bedka et al., 2018b) was retained in this work. For the filtering, thresholds for the different ambient parameters were defined based on the OT distribution for insurance loss data and microwave hail detections. The thresholds are then determined from the 2nd and 98th percentiles of the respective distribution functions. OT detections that occur outside that range are then removed to obtain the filtered OT dataset.

Ambient conditions near OT detections are interpolated spatially from the much higher resolved ERA5 reanalysis instead of ERA-Interim (25 km rather than 80 km). In contrast to the latter, ERA5 has hourly rather than 6-hourly fields, so values at the full hour are used for OT or microwave detections in the following 60 min. This reduces false filtering due to model uncertainty to resolve, for example, the rapidly evolving CAPE field with a strong diurnal cycle. For insurance loss data without a time of occurrence, we have chosen 12:00 UTC in ERA5 by default.

The bulk wind difference (near surface to 6 km) and freezing level for both microwave hail detections and insurance claims in the vicinity of OT detections are shown in Fig. 5 for South Africa and Lesotho. OTs occur at a somewhat lower 0–6 km wind difference and higher freezing level compared to microwave detections, confirming the filter choice

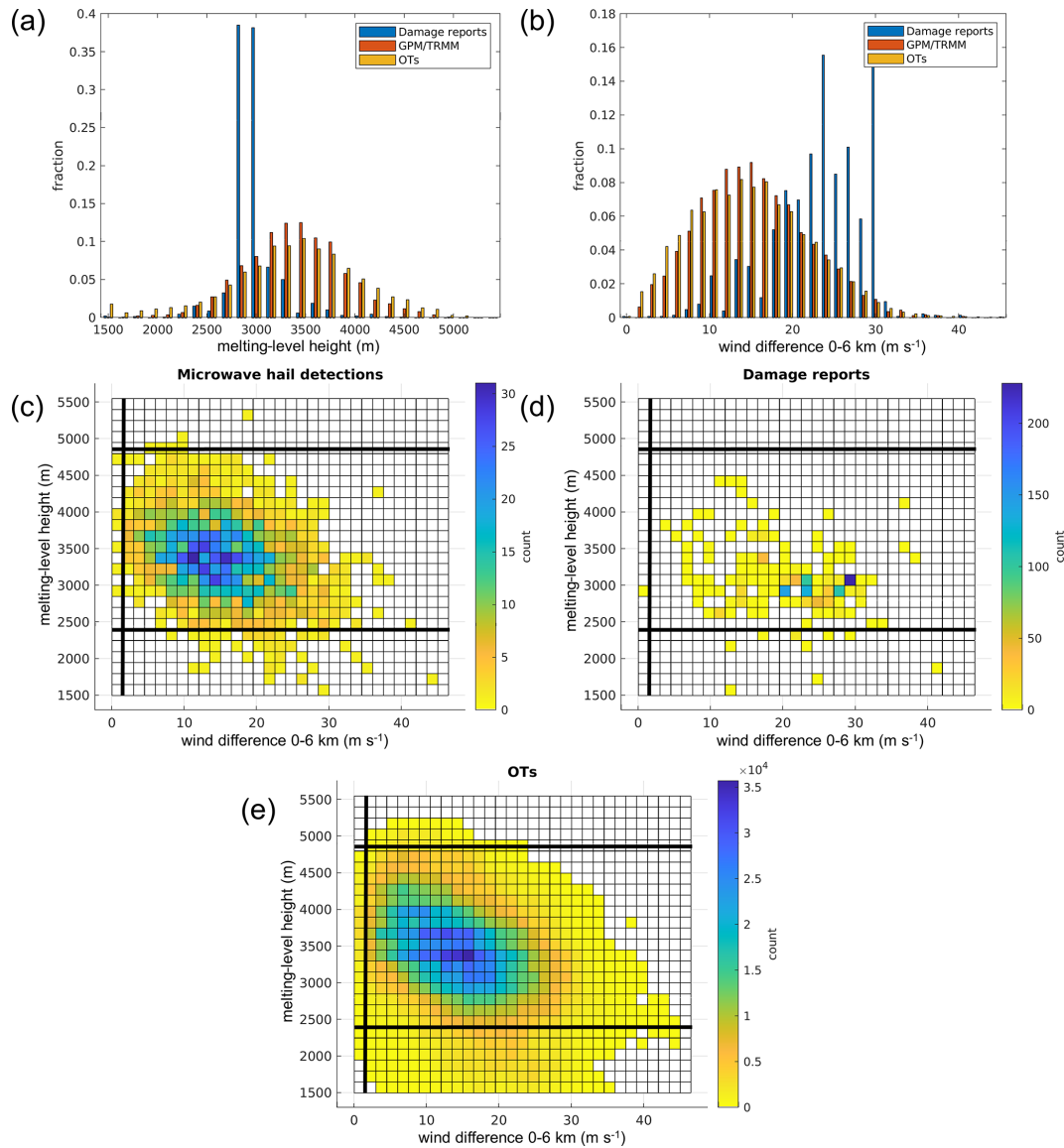


**Figure 5.** Distribution of the ERA5 0–6 km wind difference and melting-level height in hail claims (1984–2017), passive microwave detections (1998–2019), and OTs (2005–2018) for South Africa and Lesotho. **(a, b)** Probability distribution and **(c–e)** bivariate histogram for the 0–6 km wind difference and freezing level for **(c)** microwave hail detections, **(d)** damage reports, and **(e)** OT detections (bold lines indicate the selected filter thresholds; see text for further details). Only situations with positive CAPE in ERA5 were used for these computations.

in Punge et al. (2017). Note that microwave hail and OT detections occur most frequently at a 0–6 km wind difference between 10 and 20 m s<sup>-1</sup>, which represents the lower limit for organized convective storms such as multicells, supercells, or mesoscale convective storms (MCSs) to occur (e.g., Markowski and Richardson, 2010). Using a higher threshold would exclude a relevant fraction of situations where hail is likely based on the microwave algorithm. Damage reports often occur at 0–6 km wind difference between 20 and 30 m s<sup>-1</sup>, indicating a bias towards the more organized storms producing more damaging hail. But given the high concentration of these claims in populated regions, we re-

frain from using a more restrictive threshold based on this data alone. The somewhat odd distributions of damage reports shown in Fig. 5a and b are due to heavily population-biased sampling locations. As 9.5% of the OTs but only 3.5% of the microwave hail detections and 2.5% of the claims occur at a melting level of fewer than 2400 m, this altitude was used for the lower threshold with this parameter.

OT detections are thus retained if the surroundings of a given OT fulfill minimum conditions of convective instability (CAPE > 100 J kg<sup>-1</sup>), a 0–6 km wind difference > 1.5 m s<sup>-1</sup> and a height of the melting level > 2400 m (< 4845 m a.g.l.). As can be seen in the spatial distribution of the filtered OTs in

Fig. 3b, the filter removes OT detections in particular over the ocean, central Mozambique, and the Lesotho Highlands. The latter feature is due to the minimum freezing-level condition and remains to be confirmed by independent observations, for example, by hailpad or hail sensor data from the region.

A similar pattern of hail events shown in Fig. 3b is found in the global hail study by Prein and Holland (2018, Fig. 11) as well as in passive microwave data by Bang and Cecil (2019, Fig. 7; see also the discussion in the Appendix). A final judgment on the actual occurrence of significant hail on the ground would require surface observation data, such as hailpads or sensors covering multiple regions of South Africa. Such direct observation data, however, are not sufficiently available for the entire South Africa.

All subsequent analyses presented in the next sections are based on the filtered OT detections.

## 2.7 Event definition: grouping hail activity

Figure 6 illustrates the definition of historic potential events based on observed and filtered OT detections. These events are formed by computing the spatial and temporal distance between individual OT detections. OTs are assigned to the same event if they are separated by fewer than 1 h and fewer than 30 km. This simple approach can detect both single cells and other more organized forms of convection including MCSs or squall lines. Event centroids are defined as the mean latitude and longitude of the event, or grouped, OTs. An event is approximated by an ellipse and characterized by its length, width, and orientation relative to the meridian, as well as the fraction filled with OTs. In addition, we also considered the highest OT–anvil mean temperature difference among the OTs assigned to an event as a criterion for storm severity (see Sect. 3.2). Lifetime and propagation speed are estimated based on the initial and final OT detections within an event. Events can overlap when several storms pass over the same region on a given day. This actually happened in the example on 28 November 2013, shown in Fig. 6. The three events overlap, but we can assume that the activity of the smaller ones is not related to the main event, since the convection occurred several hours later when the main storm had already moved away and also was much weaker.

The event definition criteria are more restrictive compared to Punge et al. (2014), so the events are better constrained to zones of possible hail activity. Events made up by OT detections only at a single time step, hence lasting for fewer than 30 min, are neglected. In total, 33 820 events were identified from the total of 8 272 509 filtered OT detections for the entire 14-year study period. This means one event on average contains 245 individual OT detections.

Histograms of duration and propagation speed of SCS events – not considered in Punge et al. (2014) – are shown in Fig. 7. The distribution of duration is exponential in shape, in line with radar-based studies (Schmidberger, 2018; Fluck et al., 2021). While duration is roughly proportional

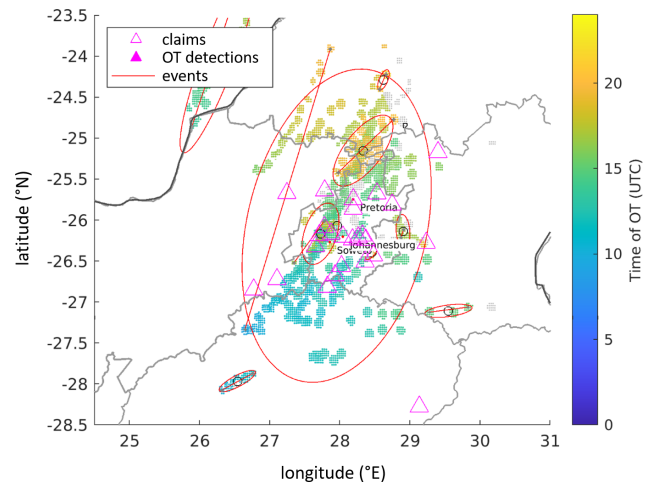


**Figure 6.** Convective storm activity in the Gauteng region of South Africa on 28 November 2013. Filtered OTs (gray dots), retained OTs (color-coded by time), hail claims (pink), and event definition (ellipses). Hail claims (magenta) indicate the location of successive hailstorms, split by the algorithm into three events, for which ellipses show the spatial extent. A line connects the locations of the initial and final OT locations, determining the orientation of the ellipse. Two smaller events overlap the main event centered over the Gauteng region, as the associated cells developed at a later time, separately from the main activity.

to length, it becomes clear that propagation speed varies over a wide range. Most frequently, the speed ranges around  $30\text{--}35\text{ km h}^{-1}$  ( $\approx 8\text{--}10\text{ m s}^{-1}$ ), slightly lower than the range of  $10\text{--}30\text{ kn}$  ( $\approx 18\text{--}55\text{ km h}^{-1}$ ) found by Carte (1966). Very high values beyond  $100\text{ km h}^{-1}$  are explained by cases where convection is triggered simultaneously over a larger area and OTs from several storms are unintendedly grouped to an event. Such unrealistic events can be simply excluded in the event set.

## 3 Stochastic modeling and event properties

In this section we describe the spatial distribution of SCS detections for the hail hazard model as well as additional event properties. This section refers to events of grouped OTs according to the event definition in Sect. 2.7. Because we cannot be assured that all historic events identified by satellite data and filtered through the ERA5 reanalysis are associated with hail on the ground, these events are hereinafter referred to as potential hail events. Distribution functions are used to approximate the historic set of potential events presented in the previous section. Stochastic events are generated using these distribution functions for relevant event properties, and 14-year samples from the stochastic event set are compared to historic data such as those available in the existing databases. The full stochastic event set covers 25 000 years with a total of 21 093 957 events spanning



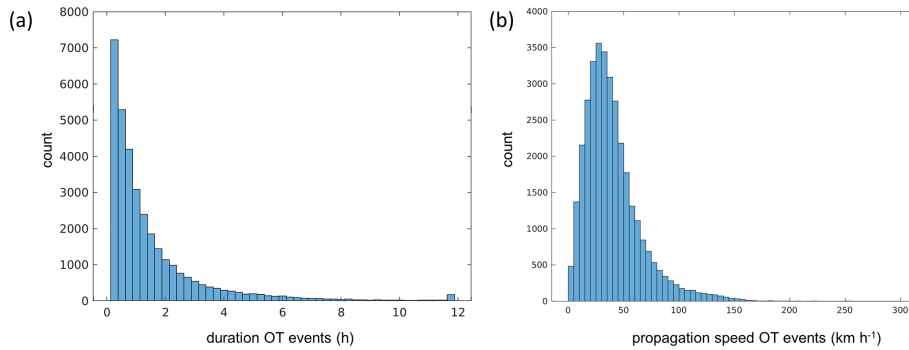


**Figure 7.** Histogram of hail-filtered OT event (a) duration and (b) propagation speed, 2005–2018.

3 442 346 d. The key challenge in generating the stochastic event set is to ensure conservation of event properties, their inter-relationships, and the spatial distribution of the historic potential hail events. This point is addressed by drawing from historic distributions using correlated random numbers where required.

The spatial distribution of potential hail events is obtained by normalizing the annual frequency of filtered OT detections, counted on a rectangular  $0.3^\circ \times 0.5^\circ$  (lat–long) grid with the average number of OTs per event (Fig. 8). This grid was chosen to retain spatial details of OT occurrence due to atmospheric processes and mechanisms, such as orographically induced lifting, but dampen local accumulations of OTs on individual pixels caused by the occasional passage of multiple storms at the same location. The implicit assumption with this method that potential hail events are distributed in the same way as OTs implies a certain amount of additional smoothing that can be neglected at scales larger than the event length.

Following Punge et al. (2014), both annual and diurnal cycles are modeled with Gaussian distributions. Approximate normal distributions were found, for example, by Allen et al. (2015) for hail reports in the US or by Taszarek et al. (2019) using ESWD reports across Europe. Even if in a few regions the annual and diurnal cycles deviate from a normal distribution due to climatological peculiarities, this distribution is plausible on average over a large area. To determine the day of year, larger grid cells of  $3^\circ \times 5^\circ$  are considered, grouping  $10 \times 10$  of the smaller grid cells used above such that the number of observations in each cell is sufficient to derive characteristics of the distribution. Depending on the mean number of OT events at a certain location, either a mixture of two Gaussians – to accommodate two peaks in spring and autumn – or a simple Gaussian distribution is fitted to the data. The relatively large grid was chosen to ensure a stable solution when fitting this complex distribution function, also in regions with few OT events. For each batch of stochastic events representing 250 years, the following procedure is applied: days are drawn from each larger grid cell of  $3^\circ \times 5^\circ$  distribution for  $N$  events in this cell and also from the respec-

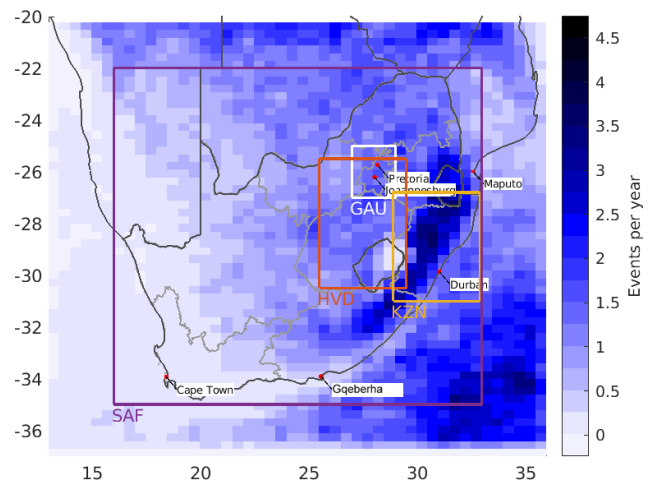


**Figure 8.** Event frequency distribution used for stochastic modeling. The boxes show different regions discussed in Sect. 3.6: the greater South Africa domain (SAF, purple box; for simplicity defined as the area between  $35$  and  $22^\circ$  S and  $16$  and  $33^\circ$  E), the Highveld (HVD, red box), and KwaZulu-Natal (KZN, yellow box) are shown as the most populated and most storm-affected regions, and the Gauteng (GAU) region is shown as the largest contiguous urban area with a significant concentration of assets.

tive eight surrounding grid cells of the same size, yielding 9 times the required number of events. To mimic the grouping of potential hail events in severe days, the same day is then attributed to blocks of  $N^{1/3}$ . The exponent of  $1/3$  was chosen to best fit the observations (1 would have all events on one day, 0 would keep the original date for each event). Finally, the day is retained for  $N$  of these events at random. The spatial smoothing technique described above effectively introduces averaging on a scale of  $9^\circ \times 15^\circ$ , which approximately represents the scale of synoptic processes and flow patterns governing the spatial (and temporal) clustering of SCS, for example, by specific weather regimes such as Baltic blocking (e.g., Mohr et al., 2019, 2020). This procedure requires only one tuning parameter and has been found empirically to

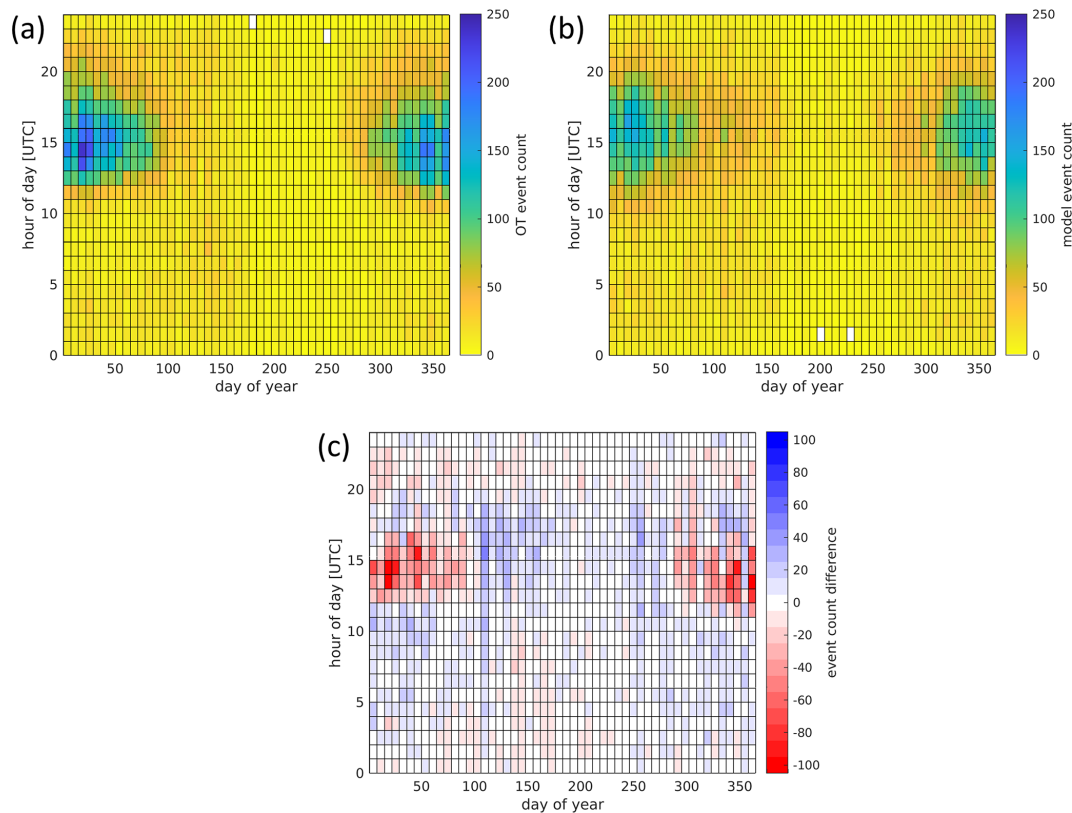


**Figure 9.** Distribution of potential hail events in the time of day and day of year: (a) historic events from 2005–2018, (b) stochastic model events, and (c) difference between the two for the events shown in Fig. 8. Days of the year are counted from 1 January. The grid shown in all figures represents 1 h and 7 d.

approximate the observed space–time distribution of days in a satisfactory manner.

The hour of day is determined in a similar way as the distribution on the larger  $3^\circ \times 5^\circ$  grid. Times are drawn from this distribution for the  $N$  potential hail events considering again a larger region of  $10^\circ \times 6^\circ$  around the grid cell center and retained with a chance of  $1/4$ . Again, the grid cell dimensions may appear arbitrary but have been carefully chosen to capture observed spatiotemporal variability. In fact, the time of day is spatially correlated at a smaller scale because in a series of potential hail events the later ones are spatially shifted with respect to the earlier ones.

Figure 9 shows the daily and seasonal variation of the (a) observed potential hail events and (b, same duration – first 14 years) the modeled events. Seasonal hail activity estimates based on OT activity (2004–2018) and passive microwave hail retrievals (1998–2018) are presented in Fig. B2. A clear maximum of the events is found in austral summer (December and January) in the afternoon around 15:00 UTC. Also note the secondary local maximum in the historic OT event set at around the day of the year 140 and at 06:00 UTC (discerned as an area of orange shades in that region in Fig. 9a), which is also represented in the model. For the Highveld region, Smith et al. (1998) report a somewhat earlier maximum

of hail events in November and December. Indeed, we find the convective season peaks around this time in the Highveld and KwaZulu-Natal and in the first half of November over Gauteng (not shown). Over the Southern Ocean, the peak occurrence is shifted towards fall. Offshore events need to be represented in the model as they can extend to the coastal region. An onshore impact of these far offshore events is quite unlikely and will be marginal at this distance.

The peak time of day is between 14:00 to 15:00 UTC or 16:00 to 17:00 South African standard time, slightly earlier than in Smith et al. (1998, 17:00–18:00) but consistent with Olivier (1990) (see also Fig. B1). The diurnal cycle is most pronounced in summer. The temporal climatologies of historic (Fig. 9a) and modeled (Fig. 9b) events match rather well. In the histograms shown in Fig. 10a and b, most of the modeled events fall within the error bars of the observed events, quantified from seven independent samples over 14 years.

### 3.1 Geometric event properties

Both length  $l$  and width  $w$  distributions, determined from the observed OT events as described in Sect. 2.7, decay rapidly with increasing values (histograms shown in Fig. 10c and d).

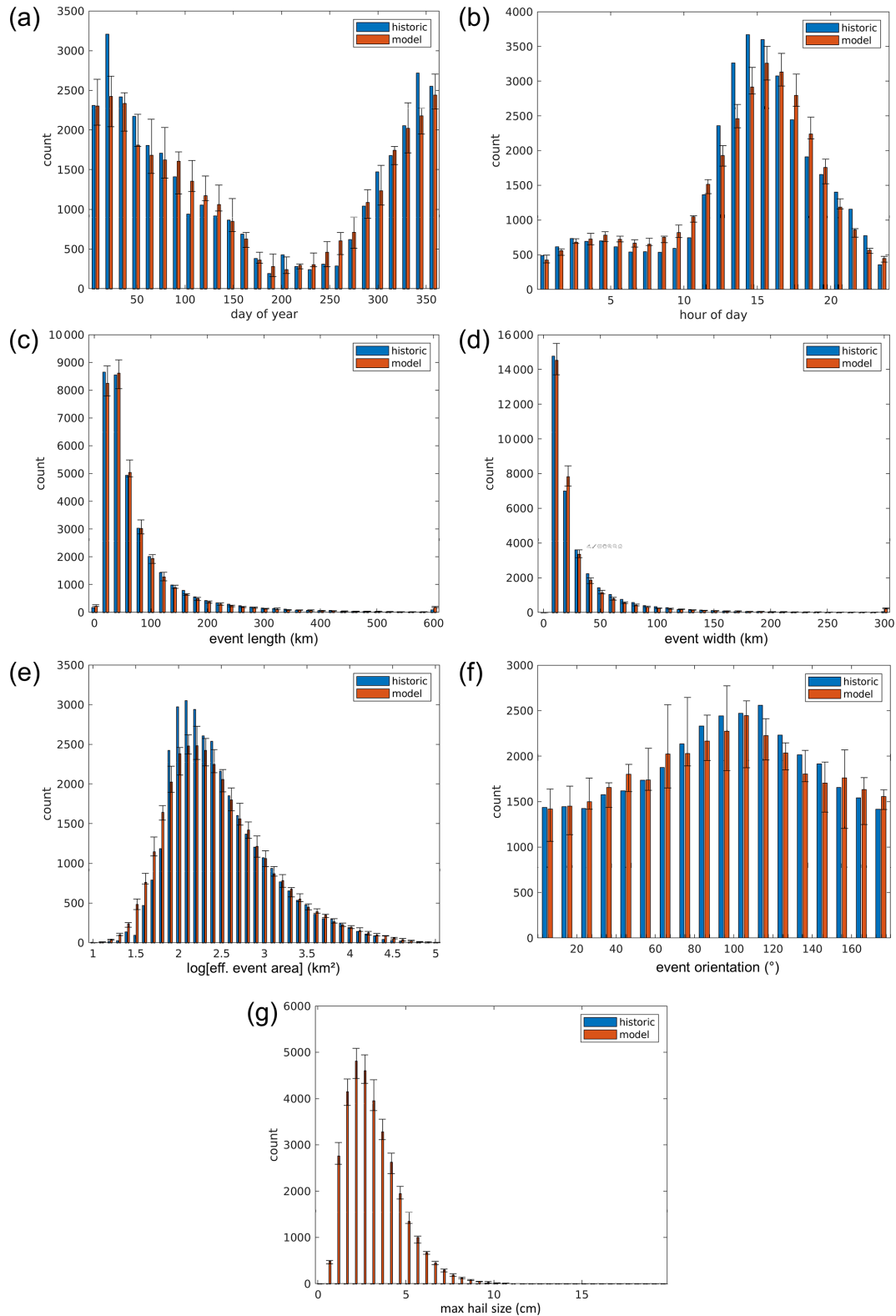


**Figure 10.** Distributions of properties of historic and stochastic events for (a) day of the year, (b) hour of the day, (c, d) event length and width, (e) affected area, (f) orientation of the events, and (g) maximum hail size. With modeled events, (error) bars indicate the median (spread) among seven independent samples of 14 years' length. Each set of bars represents 14 d, 1 h, 20 km in length, 10 km in width, 0.1 on the log scale of part (e), and 10° in orientation. Since hail severity information is essentially unknown for the historic events, blue bars are missing in (g).

**Table 1.** Potential hail event property distributions and parameters (computed with the standard MATLAB *mle* function).

Variable	Distribution	Shape parameter	Scale parameter	Location parameter
Length $l$ [km]	GEV	0.57	26.68	37.33
Width $l$ [km]	GEV	0.90	7.92	13.00
Event-to-storm-area ratio $1/f$	GEV	0.20	1.26	2.36
Hail size $d$ [cm]	Gamma	3.70	0.83	

In contrast to previous model versions, we choose to approximate both properties with generalized extreme value (GEV) distributions rather than exponential distributions. This improves their overall fit but particularly at the lower end of the range. The good match represents a use case for the GEV function family beyond extreme value theory. Positive shape parameters  $\kappa$  for length, width, and event-to-storm-area ratio (Table 1) indicate that the GEV converges to a Fréchet distribution, also known as a Fisher–Tippett Type II distribution. These distributions exhibit what are called heavy tails, meaning that the probability density function decreases rather slowly for large values of  $x$  (Wilks, 1995). Consequently, the GEV tends to give too large values, which is why length and width were truncated at 1.5 times the largest observed values at which events effectively cover the entire country (1445 km  $\times$  677 km). In addition, low widths are somewhat overrepresented, which can be attributed to the design of the event definition procedure for historic potential hail events.

The fraction  $f$  of the event area – the area of the ellipse spanned by major and minor axes of lengths  $l$  and  $w$ ,  $\pi/4lw$  – covered by OT events is also modeled using the GEV (histogram for the logarithm of the effective event area shown in Fig. 10e). Here we fitted the GEV to the inverse of that fraction, the event-to-storm-area ratio. This function was found to match observations well as the inverse has no upper bound. Furthermore, very OT-sparse events are extremely rare in the event catalogue. For the highest class ( $> 10^5$  km<sup>2</sup>), the fraction in the stochastic set is significantly higher, while the match is otherwise satisfactory. Table 1 lists the distributions and parameters for these event properties.

The orientation, or the direction of the major axis of an event, generally aligns with the direction of propagation. We find that most frequently events have an orientation of around 100°, i.e., propagate eastward to southeastward (Fig. 10f) most frequently. This, however, applies only for the whole country but not for all regions such as the high hailfall region Gauteng, where storms preferably propagate in northeasterly directions. Stochastic modeling was performed using a von Mises distribution function (Wilks, 1995).

For the sake of completeness, Fig. 10g shows the distribution of maximum hail diameters  $d^{\max}$  modeled with a gamma distribution function. As can be clearly seen, the distribution has an exponential decay for sizes larger than 2 cm. The decrease in hail counts for smaller diameters is only due to re-

porting practices and does not reflect reality. However, small hail is not relevant to hail damage and risk.

Because event properties vary across the South Africa domain, a box-window average over a 2.5° window is used to estimate these variations and to scale event properties from the historic event set. Figure 11a shows the spatial variation of event length, estimated using maximum likelihood estimation. Here the objective function is the negative logarithm of the product of the probabilities of each sample length given the assumed (GEV) distribution of lengths. The distribution parameters were then varied to find the maximum of the objective function.

Figure 11b represents the most common orientation, obtained by fitting a von Mises distribution (Mardia and Zemerch, 1975) to the regional events on a national scale. Events occurring offshore, where MCSs occur more frequently than over land (Feng et al., 2021), tend to run longer, whereas events are shorter in the western part of the domain, hinting towards less organized forms of convection. Orientation varies from southeastward in the southwest to northeastward in the northeast and is most aligned over the Eastern Cape region. Garstang et al. (1987) found winds from the northwesterly sector to prevail at 850 hPa on convective storm days in northeastern South Africa but from a much smaller sample. The larger spread in orientation towards the north and west can be explained by (i) the prevalence of storm systems affecting larger regions at the same time, hence grouping multiple parallel storms, as well as by (ii) small, quasi-stationary events whose orientation does not reflect an influence of storm propagation.

### 3.2 Storm severity indicator

At present, SCS intensity cannot be estimated accurately from geostationary satellite measurements alone, even if Marion et al. (2019) suggest that storms' tornadic intensity is related to the OT area. In a recent study, Khlopenkov et al. (2021) showed that the difference between the OT temperature and the tropopause temperature and the OT temperature and surrounding anvil in general is larger for significant severe ( $\geq 5$  cm) hailstorms than storms with smaller hail reports. But, because of the large uncertainty involved in these relationships, hail sizes estimated from the temperature differences are not further considered in our stochastic modeling approach. To at least separate days with strong convec-

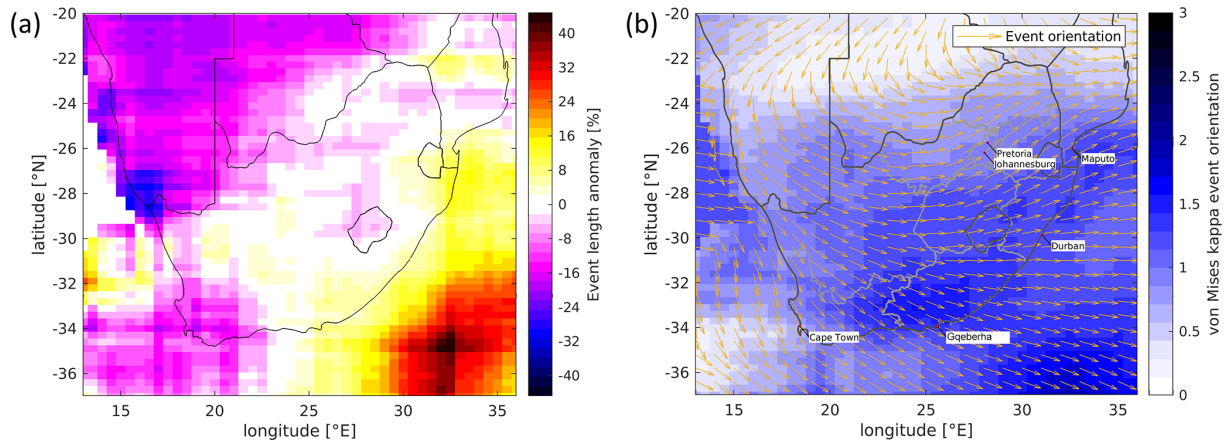


**Figure 11.** (a) Spatial variation of mean event length (%) and (b) spatial variation of event orientation, location parameter (arrows), and the shape parameter  $\kappa$  of the von Mises distribution derived from the observed OT events.

tion from fewer convective days, we determined a severity indicator based on the temperature difference between the overshooting top and surrounding anvil. This extent can be somehow related to the strength of the updraft supporting hailstone growth (Marion et al., 2019; Khlopenkov et al., 2021; Lin and Kumjian, 2022). To quantify the hail severity indicator, first the temperature difference between the OT and the surrounding anvil is computed. The severity index is then assigned to the highest such temperature difference of all OTs comprised within an event (see also discussion in the Appendix).

### 3.3 Hail size distribution in stochastic modeling

For the estimation of the damage and the risk, the hail model needs as intensity metric the hail size. Because OT data do not allow us to estimate reliable hail sizes (see previous Sect. 3.2), this quantity is only considered and implemented in the stochastic part of the model based on the hail size distributions obtained from severe weather reports. Since hail size observations in South Africa are very rare, we assume that the maximum hail diameters follow the same distribution as large hail diameters recorded in the databases of ESWD and Severe Storms Archive (see Sect. 2.3). Hail sizes for all hailswaths within an event are derived from the attributed largest hail diameter. This means that hailswaths with small hail sizes are more frequent in the stochastic model than the distribution derived from the database of maximum diameters would suggest. That is also the case in reality, as hail with a small diameter is less likely to be recorded in a database than large hail. The hailstone size distribution used in the stochastic model is assumed to be exponential as suggested by various authors using hailpad data (Sioutas et al., 2009; Berthet et al., 2011; Grieser and Hill, 2019). As we do not know the hail spectra for South Africa, this uncertainty remains in the model. However, when the final hail risk model

is calibrated using historical loss events, this uncertainty in the result can be reduced to a large degree.

### 3.4 Length–severity correlation

An important feature of the stochastic hail model is that it conserves the relation of different properties of the historic potential hail events. The most relevant properties that are correlated among each other are event length  $l$ , event width  $w$ , event severity, and fraction  $f$  of event area covered by potential hail streaks (see also Punge et al., 2014).

The scatterplot of length and width (Fig. 12a) confirms that correlations between these event properties are conserved in the model. As in Punge et al. (2014), the correlations between length and width to the storm severity indicator – represented by the minimum OT temperature difference for historic events as described in Section 3.2 – are likewise conserved here. By the same method, the fraction of the event area affected by potential hail events (“effective track area” determined from the ellipse area spanned by length  $l$  and width  $w$ ; see also Sect. 3.1) was also taken into account. This is achieved by first drawing correlated sets of random numbers for each property from a uniform distribution and determined ranks. Then, for each property, we draw values from the actual distribution, sort them, and attribute them to events using the pre-determined ranks (Punge et al., 2014).

Figure 12b shows the relation of the event length  $l$  and fraction  $f$  area, indicating that in large events, a lower fraction of the area is affected. Table 2 summarizes the Spearman rank correlation coefficients of the four variables considered. Accordingly, longer hail events tend to be wider, have a higher storm intensity, and have a lower fraction of the event area covered by hail streaks.

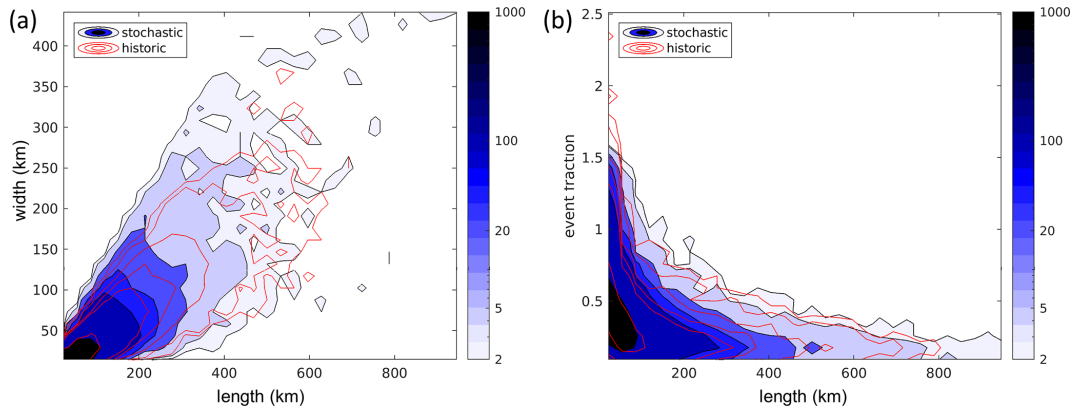


**Figure 12.** Scatterplot of historic and stochastic event properties: (a) length and width and (b) length and fraction of event covered by potential hail events.

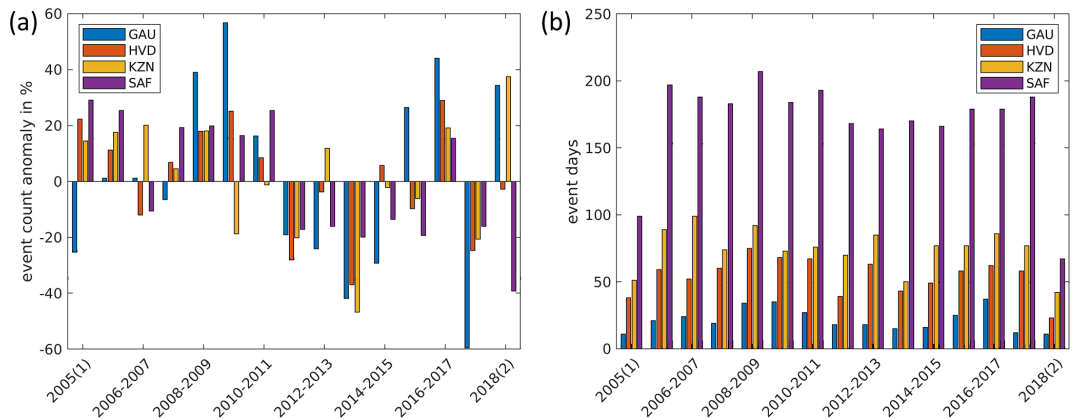


**Figure 13.** Time series of event count anomaly: (a) deviation of the annual sum from the 14-year mean and (b) event days per year (July–June) for the regions Gauteng (GAU, regional annual mean event count 35), the Highveld (HVD, 152), KwaZulu-Natal (KZN, 181), and South Africa (SAF, 1259). The July–June period is considered more appropriate as the austral summer season is not split among years. For the 2004/2005 period, only events in 2005 are covered; likewise 2018/2019 covers only the last 6 months of 2018. When computing the event count anomalies for these years, the overall repartition of events to half years was taken into account.

**3.5 Inter-annual variability**

Hailstorm frequency shows considerable year-to-year variation in both the annual number of hail events and hail days (Fig. 13). Even if there is a strong correlation between all regions shown in the figure (i.e., GAU, HVD, and KZN), smaller regions because of the short temporal and small spatial scales of potential hail events tend to experience relatively higher variability. This information helps to better understand the year-to-year variability of hail hazard and resulting losses. Note, however, that the year 2013/2014 had the second-lowest event count in the Gauteng region, despite the large damage from the 28 November 2013 event. Figure 14 shows patterns for the first 4 years of the historic event set (left), along with 5 years of the stochastic event set for a visual impression of spatiotemporal variability. Overall, the variations in location and intensity of the annual maximum look realistic. The model has fewer events in the north com-

pared to the observed event count as it is based on the scaled OT frequency instead of events, and events in this region contain fewer OTs. The modeled distribution appears overly smoothed at lower rates, but this is unlikely to be a concern.

**3.6 Intra-annual variability**

Quite relevant in practice is the representation of multiple events occurring on a single day, not considered by Punge et al. (2014). In fact, it turns out that only 15% of the potential hail event days have just one event, whereas on a few occasions, more than 30 events were detected on a single day. Figure 15 shows the number of days with a given number of observed events per day for the South Africa domain (KwaZulu-Natal – KZN, Highveld – HVD, and Gauteng – GAU regions as displayed in Fig. 15). Naturally, the smaller the study area, the lower the respective counts. Over

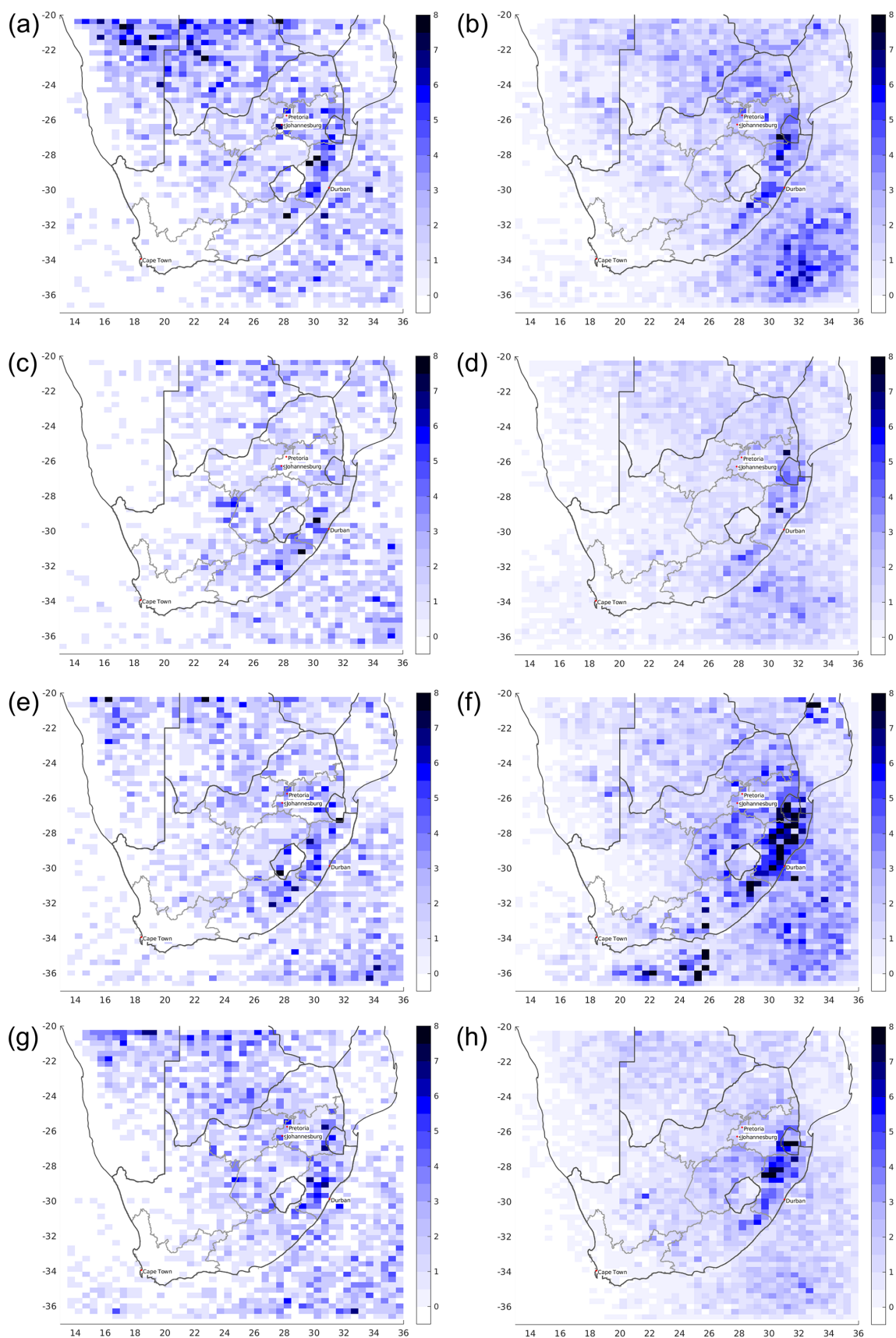


**Figure 14.** Spatial patterns of annual event distribution for single years (a, c, e, g) and the stochastic event set (b, d, f, h) for the years (a, b) 2005/2006, (c, d) 2006/2007, (e, f) 2007/2008, and (g, h) 2008/2009.

<https://doi.org/10.5194/nhess-23-1549-2023>

**Table 2.** Spearman rank correlation matrix of historic OT event properties.

Property	Set	Length	Width	Severity	Event-to-storm-area ratio
Length	historic	1.00	0.89	0.39	0.75
	model	1.00	0.90	0.39	0.49
Width	historic	0.89	1.00	0.41	0.61
	model	0.90	1.00	0.40	0.43
Severity	historic	0.39	0.41	1.00	0.17
	model	0.39	0.40	1.00	0.16
Event-to-storm-area ratio	historic	0.75	0.61	0.17	1.00
	model	0.49	0.43	0.16	1.00

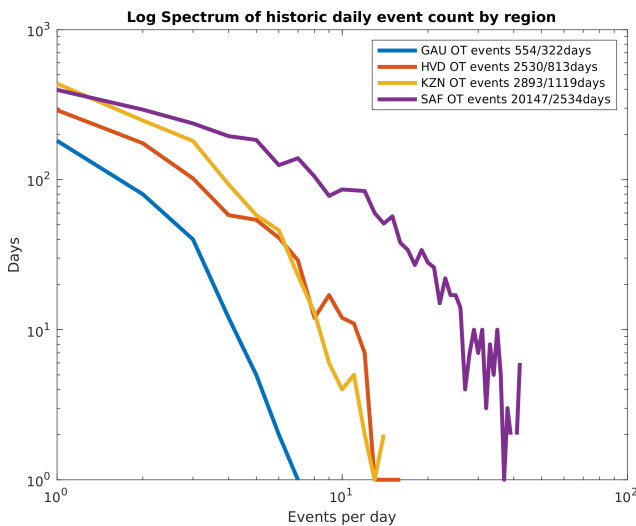


**Figure 15.** Spectrum of number of events per day on historic event days for the entire country (SAF), the Highveld (HVD), KwaZulu-Natal (KZN), and Gauteng (GAU).

the Highveld, the events are concentrated on a smaller number of days compared to the similar-sized KZN region.

The panels in Fig. 16 show the same regional frequency spectra, comparing the historic events to six equivalent subsets of the stochastic set. For example, the Highveld region has 2530 OT events over 813 d. This corresponds to around 180 hail events on 58 d each year. In an equivalent sample of subsets from the stochastic event set, the event count ranges from 2281 to 2942 ( $2523 \pm 232$ ) events on 805 to 893 d ( $838 \pm 32$ ). Table 3 summarizes the annual OT and model event statistics for the four regions.

The result is satisfactory for the South Africa and Highveld regions, whereas for the KwaZulu-Natal region, events concentrate on slightly fewer days. Given the absence of multiple-event treatment in previous model versions, this new event approach represents an improvement for the estimation of damage on individual days.

**Table 3.** Annual severe convective storm characteristics for South Africa, estimated from 14-year periods for the greater South Africa domain (SAF), KwaZulu-Natal (KZN), the Highveld (HVD), and Gauteng (GAU).

Region	OT count	OT event count	Model event count	OT days	OT event days	Model hail days
SAF	2594	1439	$1494 \pm 47$	196	181	$172 \pm 2$
KZN	359	207	$240 \pm 13$	96	80	$66 \pm 1$
HVD	339	181	$180 \pm 17$	74	58	$60 \pm 2$
GAU	71	40	$42 \pm 3$	32	23	$26 \pm 2$

In the Highveld region, there were  $74 \text{ d yr}^{-1}$  with OT detections, 58 d with OT events, and  $60 \pm 2$  events in the model event set, whereas in the Gauteng region, these numbers were 32 and 23, respectively (Table 3).

In contrast, Smith et al. (1998) found 69 hail days per year from hail reporting from a network of voluntary observers by mail for a portion of Gauteng ( $2800 \text{ km}^2$ ). The observers reported three size categories: 3–10, 11–30, and  $> 31 \text{ mm}$ ; information about the number of days for the different classes, however, is missing. Assuming an exponential hail size distribution, one can assume that the given number of hail days is dominated by events with small hail sizes. These are underrepresented in our model, as they are not relevant for hail damage. This hypothesis is supported by the fact that Smith et al. (1998) reported about severe hail ( $> 3 \text{ cm}$  in diameter) on an average of only  $3.3 \text{ d yr}^{-1}$ .

When considering only hail of this size and assuming the hail severity indicator of the stochastic event set would correspond to an actual diameter, the stochastic event set has 14.5 hail days per year in the Gauteng region. Clearly, the frequency of severe events may have changed since the time of Smith’s observations, through natural variability or climatic change, but the effect is likely small compared to the uncertainty of both past and present estimates.



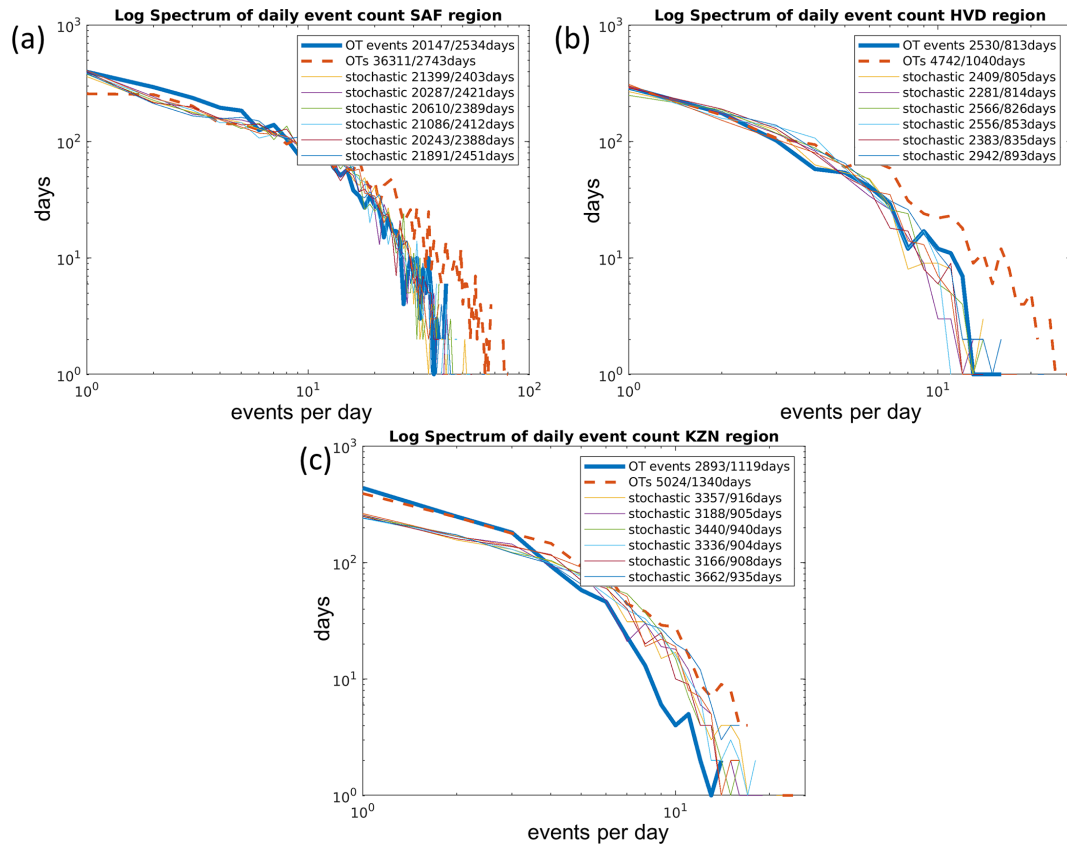


**Figure 16.** As Fig. 15, but comparing subsets of the stochastic event set to the historic OT event set (as well as the set containing events lasting only 1 time step) for each region. (a) South Africa, (b) the Highveld, and (c) KwaZulu-Natal. Numbers indicate the total count and total number of days on which these occurred for each set.

#### 4 Modeled event footprints

##### 4.1 Importance sampling

When applying the stochastic hail risk model to an insurer’s portfolio, going through millions of events for – potentially – millions of assets is a time-consuming process. While the complete event set is optimal for describing the hail hazard, an intermediate step, called importance sampling (IS), is introduced to make risk calculations more efficient, reducing the event count by a factor of approximately 10. However, the most important events in terms of damage potential are over-represented to allow for adequate statistics (notably, computing damage at higher return periods reliably).

The newly introduced explicit modeling of the date requires that all events occurring on the same day need to be considered together. Consequently, daily aggregated damage potential (here: ellipse area  $\times$  hail severity indicator) is the relevant quantity to rank event days by overall aggregated severity. The class thresholds correspond to the 50th, 80th, 95th, and 99th percentiles of aggregated severity, splitting the event set into five classes, of which 2.5 %, 7.5 %, 5 %, 10 %, and 100 % were retained. To compensate, the retained events

are attributed a higher frequency (default is once per event set period, e.g., 25 000 years), so the total damage potential is conserved. These frequency weights are hence the inverse of the retained fraction per class, i.e., 40, 13.3, 20, 10, and 1 for classes 1 to 5.

The large differences in event frequency across South Africa mean that local statistics on, for example, hail damage or probable maximum loss for a 200-year return period, can rely on a much bigger sample in the hail hotspots of the country compared to the less hail-prone regions in the west. It is hence important to retain a minimum number of events in those low-hail regions, in practice at least one per 250-year batch (if one is present in the first place).

Figure 17 illustrates this point: Fig. 17a shows the distribution of events retained in the importance sampling; some areas in the west and far north have fewer than 50 events in a  $0.5^\circ \times 0.3^\circ$  box ( $\approx 30$  km in extent). As to be expected, when frequency weights are applied (Fig. 17b and c), the distribution corresponds very well to that of the full event set (Fig. 8).

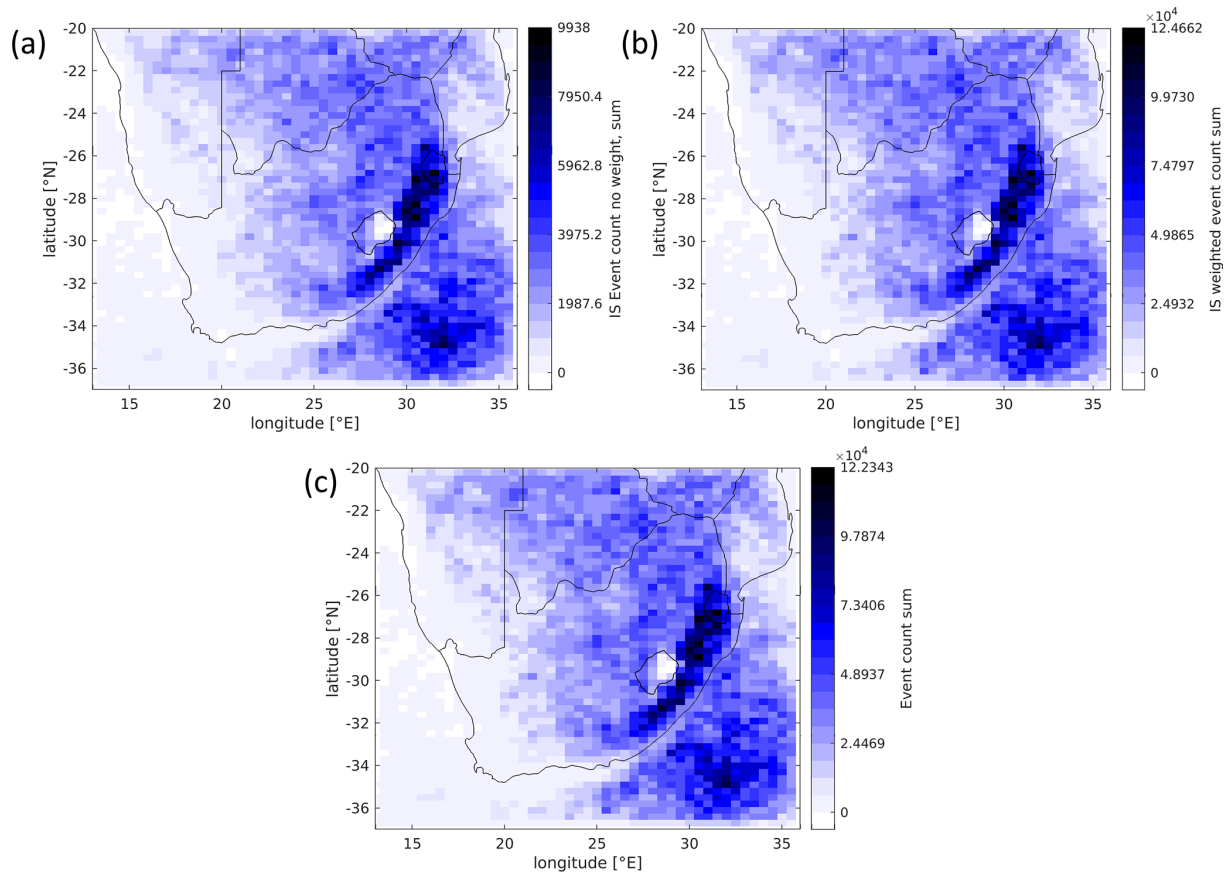


**Figure 17.** (a) Number of events retained by the importance sampling; (b) as (a) but weighed by frequency; (c) event frequency before importance sampling.

## 4.2 Footprint generation

Finally, the areas affected by hail with corresponding hail sizes need to be determined for the stochastic events, forming a hail “footprint”. Given the arbitrary paths of thunderstorms observed for the historic events, we chose to achieve this by a randomized process of allocating ellipsoid hail streaks within the event area. These streaks are aggregated across all events of a day to form the daily hail footprint, which is applied to portfolios in the further stages of the risk model. The footprint catalog gives local information on hail occurrence and a severity indicator for each day on a  $2 \times 2 \text{ km}^2$  grid covering continental South Africa.

The footprint generation algorithm attempts to mimic observed patterns of hailfall in an empirical way. A first streak is located in the center of the event, and its length, orientation, and severity indicator match those attributed to the event. Streak widths were chosen to approximate hail streaks in ground- and radar-based studies (Stout et al., 1960; Changnon, 1977; Schmidberger, 2018; Fluck et al., 2021), without strictly following observed distributions. An exponential distribution is assumed, with a mean width of 6 km and a maximum of 20 km. Hail severity decreases towards

the streak’s edges in a parabolic way, as proposed by Schmidberger (2018). This is deemed acceptable, since actual hail patterns on the ground are largely uncertain across the world. In an iterative process, further streaks are added until the combined streak area covers the prescribed fraction of the event area. They are located randomly within the event area, and the possible event length decreases with each new streak. Streak orientation is varied by  $\pm 10^\circ$  around the event orientation to account for both the uncertainty in the tracking of OTs and new cell formations preferably at the downshear flank.

Accumulating events over a time equivalent of 2500 years, Fig. 18a and b show the number of events hitting each cell for a 10 % sample of the importance-sampled event set, for the least and most severe class (1 and 5, respectively). Clearly, the footprint frequency over the Highveld and KwaZulu-Natal increases from class 1 to 5, whereas it decreases in the western half of the country. Consequently, hailstorms are relatively more often severe over the Highveld than other parts of the country, with important consequences for the financial risks associated with the peril. Figure 18c shows the accumulated, frequency-weighted annual sum of hail occurrences in the model. We note that the local frequency-weighted hail count per year is about 2 in the KwaZulu-Natal

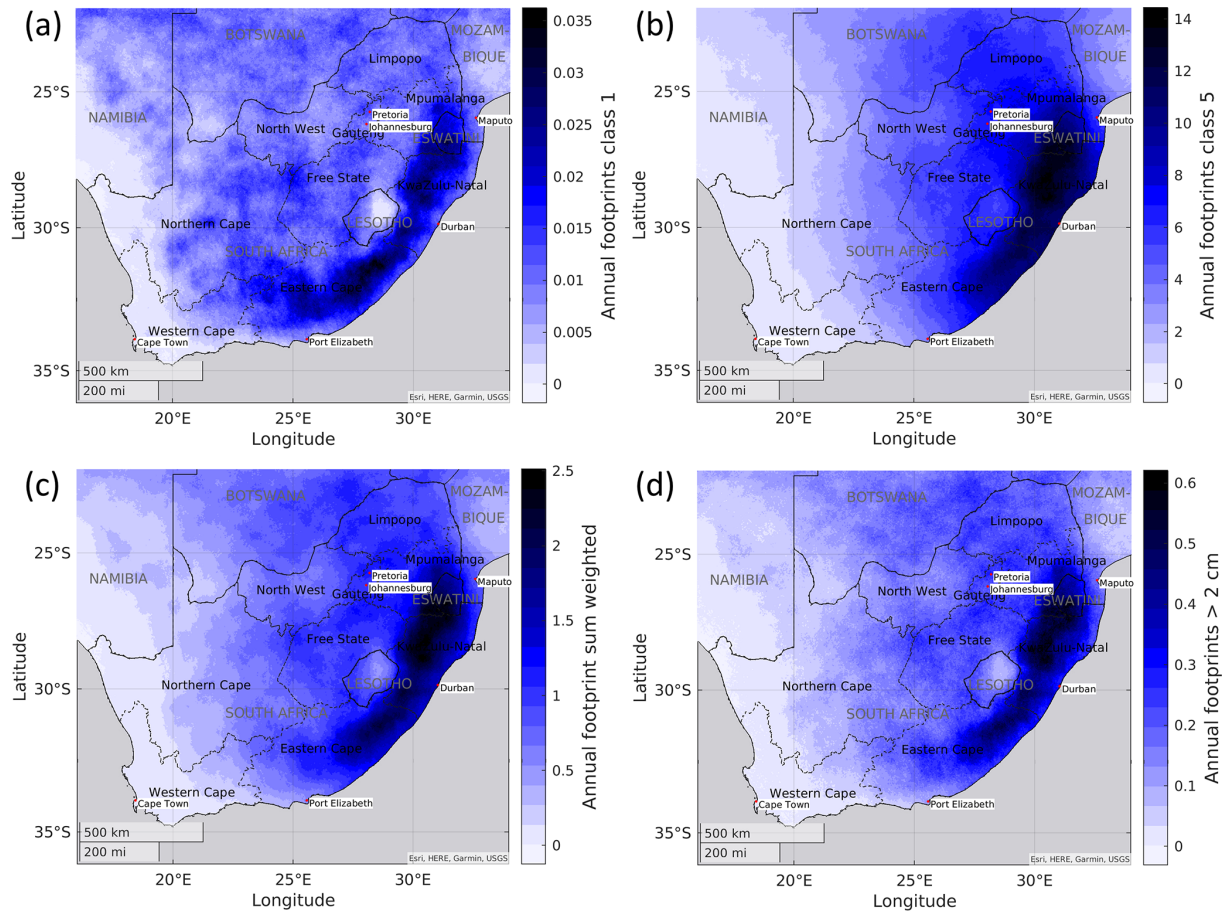


**Figure 18.** Number of events hitting a grid cell per year (a, b): for classes 1 and 5, respectively; (c) total, frequency-weighted; (d) as (c) but for hail diameter > 2 cm. Port Elizabeth is now Qqeberha.

maximum and around 1 in the Highveld and Gauteng regions, roughly in line with 0.81 normalized hail days per year in Held (1974). For a maximum hail severity indicator greater than 2 cm, the overall number of events decreases by about 75 %, while the overall spatial distribution remains almost the same (Fig. 18d).

Based on the local hail count and event set length, return periods, i.e., inverse frequencies, can be estimated for given hail severity thresholds. Hail severity for a fixed return period was calculated by linear interpolation between such thresholds fixed at constant intervals. Summarizing the information contained in the event set, and assuming hail severity estimates were corresponding to actual hail sizes, Fig. 19 shows the maximum hail severity that can be expected once per decade at a given location: in the most affected parts in the east, near Newcastle and Ladysmith, hailstones of around 4 cm were to be expected, followed by 3.5 cm in Pietermaritzburg, Mthatha, or Nelspruit (officially known as Mbombela); 3.1 cm in Durban; and 2.8 cm in the major cities of Gauteng but fewer than 2 cm in the western third of the country. Despite the uncertainty regarding the

exact hail-size–OT relation, this information has clear implications for the need for mitigation measures to reduce hail risk, such as roof-cover robustness or covered parking of vehicles.

## 5 Conclusions

In our paper, we have presented a method to estimate hail frequency for South Africa, a country frequently affected by large hail, and to generate footprints over a long-term period of 25 000 years, which can be used by the insurance industry to quantify hail risk. Despite the high exposure to hail, no reliable estimates of hail frequency are available for South Africa to date. The lack of available damage reports or accurate hail observations, for example, by human observers or by hailpad observations, limits the accuracy of hail hazard descriptions (compared to, e.g., Europe, Púčik et al., 2019). The uneven distribution of population and wealth in the country complicates this matter further. For this reason, satellite-based observations of SCS/hailstorms have been used to describe the spatial distribution and nature of intense convec-

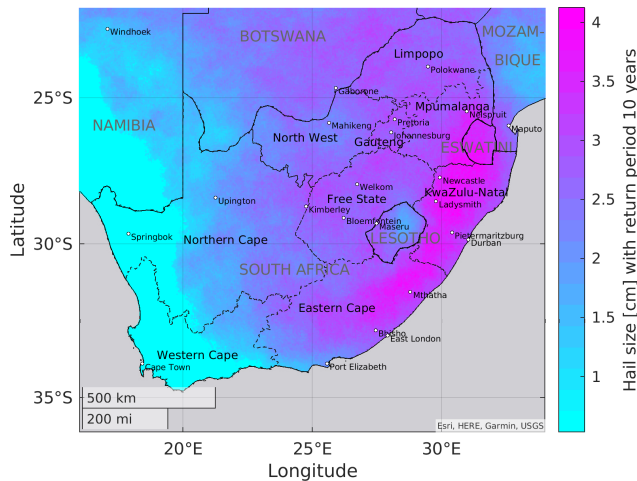


**Figure 19.** Model-estimated maximum hail size occurring once in 10 years for grid cells across South Africa, computed as the lowest hail diameter class with a return period. Port Elizabeth and Nelspruit have been renamed to Gqeberha and Mbombela, respectively.

tion in the country. By stochastic modeling, hail hazard was derived from a large sample of events, which can be used to quantify hail risk for a given portfolio of insured assets. As was shown in the paper, the stochastically generated event set matches very well with the historic event set over a 14-year period.

The combination of improved OT detection and advanced spatiotemporal clustering allows the determination of hail hazard zones much more precisely compared to the method used for the Willis European Hail Model (Punge et al., 2014). Regarding storm properties, exponential distributions have been replaced by GEV distributions in most instances, yielding a better fit to observations.

More importantly, the model is now capable of producing realistic spatiotemporal distribution of events, handling multiple events per day as well as their spatial spread and multi-year variability. By explicitly including the date as an event property, it has become possible to represent outbreaks with multiple events on a single day in a realistic way (see Fig. 16). Hence the increased financial risk of clusters with repeating severe storms (e.g., 11 and 28 November 2013 in Gauteng, Dyson et al. (2020); or in Germany on 27–28 July 2013, Kunz et al. (2018); Munich RE (2015)) is accounted for.

In addition, the footprint generation algorithm has been revised to predict hail only in a fraction of the event area, mimicking observed storms. This will assist in the calibration of the exposure and vulnerability functions of the risk model and yield more accurate loss estimates. Finally, another addition compared to previous model versions is the time of day, which will allow for the reflectance of daily changes in exposure, for example of parked cars, in the risk model.

Of course, with the OT-based approach, some scattered, short-lasting hail episodes forming smaller hailstones may be missed. These events, however, are generally unimportant for the hail threat to insurance businesses, which are mostly concerned about major loss events. Another limitation of the OT approach is the difficulty to distinguish hail-producing from non-hail producing storms or to identify the fraction of an individual storm's track in which it produces hail. While storm environments from reanalysis (e.g., Bedka et al., 2018b; Punge et al., 2017) can help with the first task, they can hardly address the second.

Nonetheless, while the absolute number of hail days per year strongly depends on the minimum size of hail considered, findings are comparable to local hail-reporting-based studies, particularly for the Gauteng region, for which some studies of observed hail frequency are available (Carte, 1977; Admirat et al., 1985; Smith et al., 1998). However, there is disagreement with previous studies over the presence of a hail frequency maximum in the Lesotho mountains, absent in our study. Also, there is uncertainty in the occurrence of hail offshore, albeit not in the focus of this study. Future studies will have to address whether the differences between our study and previous work in the spatial distribution of hail are artifacts of imperfect methodology and assumption or actually represent reality.

## Appendix A: OT intensity

To demonstrate the relationship between IR-based storm-intensity metrics and an estimate of hail size, we compared GOES-12 and GOES-13 data with the 95th percentile Maximum Expected Size of Hail (MESH95) from the US NEXRAD GridRad dataset at hourly intervals from 2007–2017 (Murillo and Homeyer, 2019). MESH95 cell objects exceeding two pixels in area ( $10 \text{ km}^2$ ) and spaced by at least 28 km are derived using watershed segmentation applied to the hourly 10 mm+ MESH95 climatology (Murillo and Homeyer, 2019) using the open-source Tracking and Object-Based Analysis of Clouds (tobac v1.2; Heikenfeld et al., 2019) Python package. Further, following Murillo et al. (2021), we have applied linear discriminant analysis (LDA) using their coefficients to combine reanalysis precipitable water and 0–6 km shear to filter out likely false alarms.

In Fig. A1, the following GOES-12/13 IR-derived parameters are matched with and binned by MESH95 cell maxima: OT probability, area of the embedded cold spot (ECS), ECS–anvil temperature difference, and ECS–tropopause temperature difference. Though there is considerable overlap in GOES parameters between the various MESH95 bins, it can be seen that all parameters representing updraft intensity and area are positively correlated with MESH95. The correlation between GOES-16 data and MESH95 during spring and summer 2017 (not shown) is even greater than GOES-13, due to higher spatial resolution of GOES-16. OT prob-

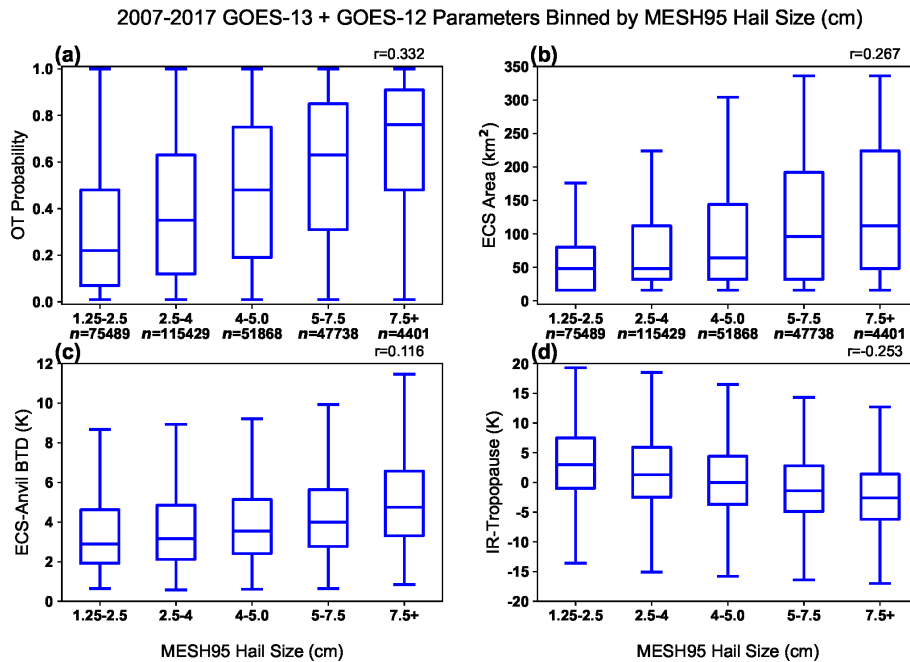
ability is better correlated with MESH95, suggesting that the prominence of an ECS relative to the background anvil combined with its intensity and area are all contributing to higher OT probability. Therefore, the IR–anvil brightness temperature difference is a suitable parameter, independent of any reliance on a numerical model, for purposes of modeling the expected hail severity at the ground. Though these results suggest a quasi-linear relationship between MESH- and satellite-derived updraft intensity proxies, the true relationship between such proxies and hail size encountered on the ground is unknown, primarily due to known uncertainties with hail size reporting. While direct matching of SEVIRI with MESH cells over South Africa is not possible, the  $\approx 3$  km nadir pixel resolution (halfway between GOES-13 and GOES-16) and lower view zenith angles over the South African domain (MSG is positioned at  $0^\circ$  E) are expected to result in similarly robust correlations with hail size diameter.

Table A1 further compares the frequency of GOES-13, GOES-16, and MSG ECS detections, e.g., areas that appear distinctly colder than the surrounding anvil and are considered to be OT candidates, and OT detections (OT probability  $\geq 0.5$ ) matching various hail detections from radar cells, ground-spotter-reported hail size (SPC), and microwave radiometer (MWR) hail detections. Requiring OT probability  $\geq 0.5$  to refine severe hail detections to those we are most confident in, we lose 54 % (44 %) of the severe-hail-producing storms exceeding 4 cm MESH95 maxima for GOES-13 (GOES-16). In other words, many severe hailstorms can look quite “boring” from a satellite infrared perspective, but the boring ones are hard to differentiate from false OT detections in anvils (i.e., detections in cold outflow near to real OTs). Uncertainty between report time or the time a radar scanned a storm vs. the time of OT detections may also influence our results. For example, an OT may have been prominent several minutes before the time of a hail detection, but we only have a single GOES snapshot to match. By relaxing the matching criterion to ECS detections, we lose only 30 % (17 %) of likely severe-hail-producing cells for GOES-13 (GOES-16).

The frequency of geostationary updraft detections that are co-located with MWR hail detections is comparable to MESH95 and SPC hail reports despite added uncertainty due to parallax shifts in the storm positions in microwave data, especially those close to the limb of the overpass. Enabled by the global coverage of MWRs, Table A1 shows that 2005–2018 MSG SEVIRI ECS and OT detections over South Africa match with likely severe MWR hail detections with frequencies similar to GOES-16 over the US. Although the total number of matches is relatively low over South Africa, this suggests that MSG IR-based updraft detections agree with independent hail detections, thus, supporting the use of MSG SEVIRI to detect hail cores over South Africa.

**Table A1.** Detection counts and fractions of geostationary-derived embedded cold spot (ECS) and OT detections matched within 28 km<sup>2</sup> and 15 min of hail observations.

	Count	Count with ECS	Fraction with ECS	Count with OT	Fraction with OT
<b>GOES-13</b>					
MESH95 ≥ 4 cm	148 326	104 007	0.70	67 668	0.46
MESH95 ≥ 2.5 cm	384 444	219 436	0.56	109 839	0.29
SPC hail ≥ 2.5 cm	121 505	82 443	0.68	46 211	0.38
MWR P_hail ≥ 50	4225	3165	0.75	2440	0.58
<b>GOES-16</b>					
MESH95 ≥ 4 cm	10 452	8677	0.83	5814	0.56
MESH95 ≥ 2.5 cm	28 811	19 367	0.67	10 619	0.37
<b>MSG</b>					
MWR P_hail ≥ 50	732	536	0.73	458	0.63



**Figure A1.** GOES-12 and GOES-13 IR-based parameters binned by MESH95 hail sizes. MESH95 exceeding 4 cm is considered a potentially severe storm. Counts in each bin are shown below the x axis, and the Pearson correlation coefficient is shown in the upper right of each panel.

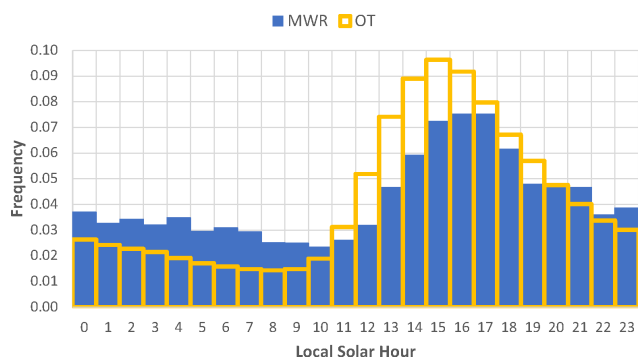


**Figure B1.** Variation in OT activity throughout the day, estimated with the OT method (yellow) and passive microwave detection (blue), normalized by the total number of detections.

## Appendix B: Climatology of satellite-derived hail estimates

The microwave hail detection algorithm (Bang and Cecil, 2019) and the OT-based detection method (Khlopenkov et al., 2021) have independently been designed to represent hail occurrence. A comparison of the spatial and temporal variability of the detected occurrences can thus be used to identify times and locations where the two methods disagree, indicating potential weaknesses or imbalances in one of the approaches.

The daily cycle of OT activity is more pronounced compared to that for the microwave detection (Fig. B1), and its maximum sets in almost an hour earlier. Overall the agreement between the two satellite climatologies, however, is very good, but the OT algorithm may be slightly too sensitive for weaker convection.

To that end, Fig. B2 shows the seasonal sums of OT (Fig. B2a–d) and microwave (Fig. B2e–h) activity over the respective observational period. Of all seasons, most OTs are detected over land in austral summer (DJF; Fig. B2a and e), and the spatial distribution is similar to that of climatology. In autumn (MAM; Fig. B2b and f), and to a lesser degree in winter (JJA; Fig. B2c and g), both methods indicate persisting hail activity over the eastern oceans and along the coast. Summertime (JJA; Fig. B2c and g) presents the highest activity with both methods and a clear focus along the eastern slopes of the Great Escarpment and some activity over the southeastern ocean. We note a difference in the north, where the OT algorithm appears to detect intense but, due to high temperatures, non-hail-producing convection (Fig. B2c). Both methods indicate widespread hail activity in spring (SON; Fig. B2d and h) over the eastern half of the continent and adjacent oceans, with a somewhat more pronounced concentration around Botswana and the Drakensberg with the OT method. This method could thus be somewhat too sensitive to the frequent but weak convective activity in springtime also found in other regions of the world (e.g., Europe, Punge et al., 2017).

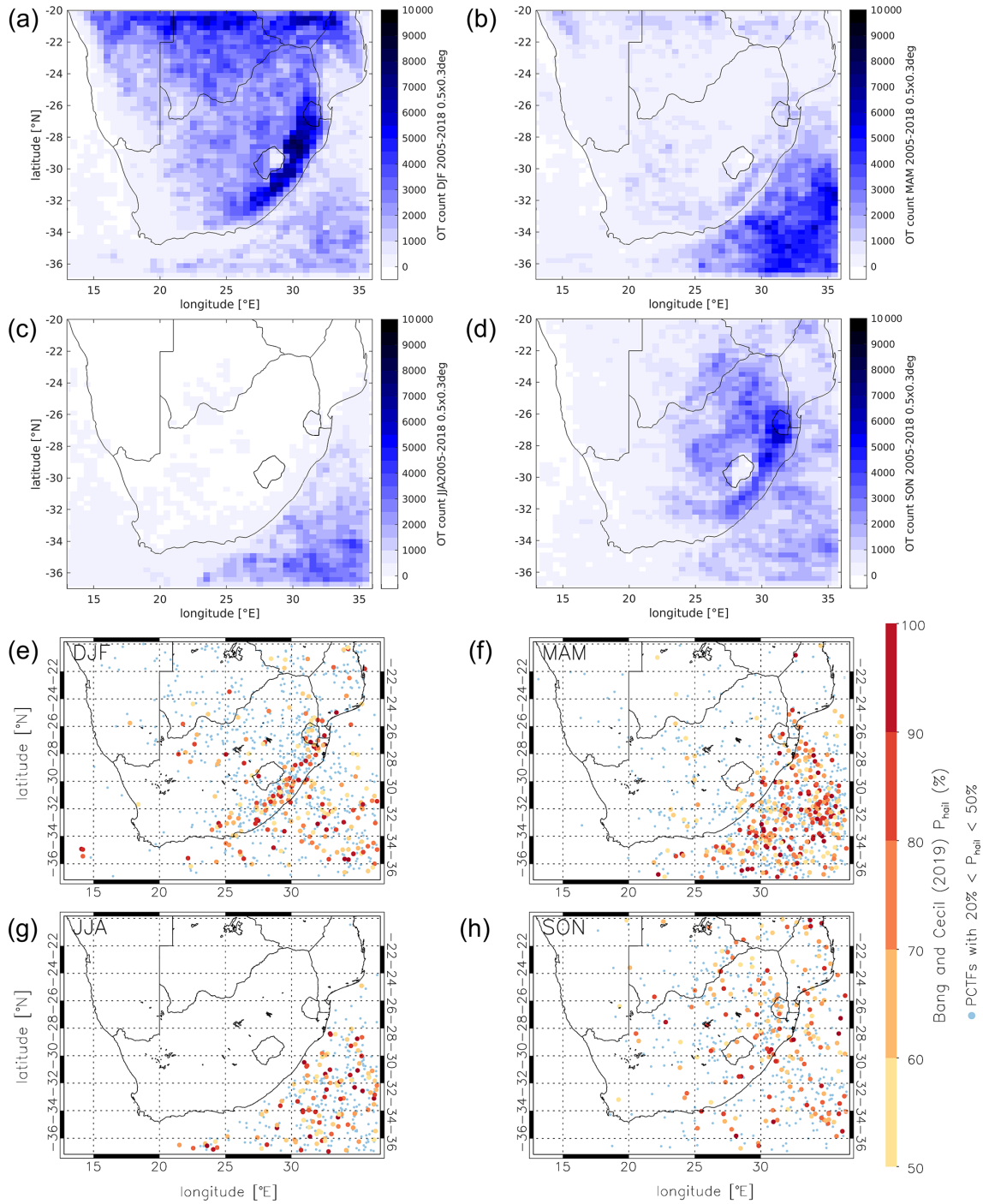


**Figure B2.** Seasonal hail activity estimates based on overshooting top activity (2004–2018, **a–d**) and passive microwave hail retrievals (1998–2022, **e–h**) for austral summer (DJF; **a, e**), autumn (MAM; **b, f**), winter (JJA; **c, g**), and spring (SON; **d, h**).



*Code availability.* The hail event identification and stochastic generation software was developed in partnership with insurance broker Willis Towers Watson (WTW) and is therefore not publicly available.

*Data availability.* MSG SEVIRI data are available from EUMETSAT: <https://www.eumetsat.int/eumetsat-data-centre> (EUMETSAT, 2023). The OT dataset is not publicly available, but it may be available upon request.

The GPM GMI and TRMM TMI L1C passive-microwave data are available for download from the Precipitation Processing System (<https://arthurhouhttps.pps.eosdis.nasa.gov/https://arthurhouhttps.pps.eosdis.nasa.gov/>; last access: 21 April 2023) after registration (<https://registration.pps.eosdis.nasa.gov/registration/>, last access: 21 April 2023).

The GOES-13 and GOES-16 data used to generate ECS and OT detections over the US can be acquired from the NOAA Comprehensive Large Array-Data Stewardship System (CLASS): <https://www.avl.class.noaa.gov/saa/products/welcome.jsessionid=BDF491314248B818A20B53DFF3EC97B5> (NOAA, 2023).

The GridRad MESH data used to analyze hailstorm detectability over the US can be acquired from <http://gridrad.org/data.html> (University of Oklahoma, 2023).

ERA5 reanalysis can be downloaded from the Copernicus Climate Change Service (C3S) Climate Data Store (<https://cds.climate.copernicus.eu/#!/search?text=ERA5&type=dataset;Copernicus,2023>).

Hail reports are available at the European Severe Weather Database (ESWD) operated by ESSL: <https://eswd.eu/> (ESWD, 2023; Dotzek et al., 2009).

Insurance loss data and hail reports for Australia are not publicly available.

*Author contributions.* HJP, MK, SDB, and KMB conceived the stochastic model and this study. KMB designed the OT detection algorithm, provided OT data, and suggested figures. MK supervised the model design and development. SDB developed the microwave hail-detection algorithm and provided the corresponding data. KFI evaluated the OT algorithm against radar data. HJP analyzed the data and prepared the manuscript, with all co-authors providing critical feedback and helping shape the analysis and manuscript.

*Competing interests.* The contact author has declared that none of the authors has any competing interests.

*Disclaimer.* Publisher's note: Copernicus Publications remains neutral with regard to jurisdictional claims in published maps and institutional affiliations.

*Acknowledgements.* We thank ECMWF for providing ERA5 reanalysis data and Willis Towers Watson (WTW) for providing hail damage claims for sample events. We thank the Data Center at the University of Wisconsin-Madison, Space Science and Engi-

neering Center, for providing the archived MSG SEVIRI imagery used in this paper. We thank the European Severe Storms Laboratory (ESSL) and the Australian Bureau of Meteorology for providing hail report data. Credit is given to <https://gadm.org/> (last access: 21 April 2023) and <https://www.geonames.org/> (last access: 21 April 2023) for providing geodata used to produce the maps.

*Financial support.* This research has been supported by the Helmholtz Association (Research Program “Changing Earth – Sustaining our Future”), the Center for Disaster Management and Risk Reduction Technology (CEDIM), the NASA Applied Sciences Disasters program award (18-DISASTER18-0008), by WTW through the Willis Research Network (Willis Fellow Punge), and by the German Research Foundation (DFG) – project ID 257899354 – TRR 165 (Waves to Weather) within the subproject B1 (Michael Kunz).

The article processing charges for this open-access publication were covered by the Karlsruhe Institute of Technology (KIT).

*Review statement.* This paper was edited by Gregor C. Leckebusch and reviewed by Ansie Smit and Rebecca Adams-Selin.

## References

- Adler, R. F., Markus, M. J., and Fenn, D. D.: Detection of Severe Midwest Thunderstorms Using Geosynchronous Satellite Data, *Mon. Weather Rev.*, 113, 769–781, [https://doi.org/10.1175/1520-0493\(1985\)113<0769:DOSMTU>2.0.CO;2](https://doi.org/10.1175/1520-0493(1985)113<0769:DOSMTU>2.0.CO;2), 1985.
- Admirat, P., Goyer, G. G., Wojtiw, L., Carte, E. A., Roos, D., and Lozowski, E. P.: A comparative study of hailstorms in Switzerland, Canada and South Africa, *J. Climate*, 5, 35–51, <https://doi.org/10.1002/joc.3370050104>, 1985.
- Allen, J. T., Tippet, M. K., and Sobel, A. H.: An empirical model relating U.S. monthly hail occurrence to large-scale meteorological environment, *J. Adv. Model. Earth Syst.*, 7, 226–243, <https://doi.org/10.1002/2014MS000397>, 2015.
- Allen, J. T., Giammanco, I. M., Kumjian, M. R., Punge, H. J., Zhang, Q., Groenemeijer, P., Kunz, M., and Ortega, K.: Understanding Hail in the Earth System, *Rev. Geophys.*, 58, e2019RG000665, <https://doi.org/10.1029/2019RG000665>, 2020.
- Ayob, N.: Hail nowcasting over the South African Highveld, MS thesis, North-West University, South Africa, <https://repository.nwu.ac.za/handle/10394/33836> (last access: 21 April 2023), 2019.
- Bang, S. D. and Cecil, D. J.: Constructing a Multifrequency Passive Microwave Hail Retrieval and Climatology in the GPM Domain, *J. Appl. Meteorol. Clim.*, 58, 1889–1904, <https://doi.org/10.1175/JAMC-D-19-0042.1>, 2019.
- Bang, S. D. and Cecil, D. J.: Testing Passive Microwave-Based Hail Retrievals Using GPM DPR Ku-Band Radar, *J. Appl. Meteorol. Clim.*, 60, 255–271, <https://doi.org/10.1175/JAMC-D-20-0129.1>, 2021.

- Bedka, K., Brunner, J., Dworak, R., Feltz, W., Otkin, J., and Greenwald, T.: Objective Satellite-Based Detection of Overshooting Tops Using Infrared Window Channel Brightness Temperature Gradients, *J. Appl. Meteorol. Clim.*, 49, 181–202, <https://doi.org/10.1175/2009JAMC2286.1>, 2010.
- Bedka, K., Allen, J., Punge, H., and Kunz, M.: A Long-Term Overshooting Convective Cloud Top Detection Database Over Australia Derived From MTSAT Japanese Advanced Meteorological Imager Observations, *J. Appl. Meteorol. Clim.*, 57, 937–951, <https://doi.org/10.1175/JAMC-D-17-0056.1>, 2017.
- Bedka, K., Murillo, E., Homeyer, C. R., Scarino, B., and Mersiovsky, H.: The Above Anvil Cirrus Plume: An Important Severe Weather Indicator in Visible and Infrared Satellite Imagery, *Weather Forecast.*, 33, 1159–1181, <https://doi.org/10.1175/WAF-D-18-0040.1>, 2018a.
- Bedka, K. M., Allen, J. T., Punge, H. J., Kunz, M., and Simanovic, D.: A long-term overshooting convective cloud-top detection database over Australia derived from MTSAT Japanese advanced meteorological imager observations, *J. Appl. Meteorol. Clim.*, 57, 937–951, <https://doi.org/10.1175/JAMC-D-17-0056.1>, 2018b.
- Bedka, K. M.: Overshooting cloud top detections using MSG SEVIRI Infrared brightness temperatures and their relationship to severe weather over Europe, *Atmos. Res.*, 99, 175–189, <https://doi.org/10.1016/j.atmosres.2010.10.001>, 2011.
- Bedka, K. M. and Khlopenkov, K.: A probabilistic multispectral pattern recognition method for detection of overshooting cloud tops using passive satellite imager observations, *J. Appl. Meteorol. Clim.*, 55, 1983–2005, <https://doi.org/10.1175/JAMC-D-15-0249.1>, 2016.
- Berthet, C., Dessens, J., and Sanchez, J.: Regional and yearly variations of hail frequency and intensity in France, *Atmos. Res.*, 100, 391–400, <https://doi.org/10.1016/j.atmosres.2010.10.008>, 2011.
- Carte, A.: Hail damage to agriculture and its prevention, *S. Afr. J. Sci.*, 73, 327–330, 1977.
- Carte, A. E.: Features of Transvaal hailstorms, *Q. J. Roy. Meteorol. Soc.*, 92, 290–296, <https://doi.org/10.1002/qj.49709239214>, 1966.
- Cecil, D. J.: Passive Microwave Brightness Temperatures as Proxies for Hailstorms, *J. Appl. Meteorol. Clim.*, 48, 1281, <https://doi.org/10.1175/2009JAMC2125.1>, 2009.
- Changnon Jr., S. A.: The scales of hail, *J. Appl. Meteorol.*, 16, 626–648, [https://doi.org/10.1175/1520-0450\(1977\)016<0626:TsoH>2.0.CO;2](https://doi.org/10.1175/1520-0450(1977)016<0626:TsoH>2.0.CO;2), 1977.
- Cintineo, J. L., Smith, T. M., Lakshmanan, V., Brooks, H. E., and Ortega, K. L.: An Objective High-Resolution Hail Climatology of the Contiguous United States, *Weather Forecast.*, 27, 1235–1248, <https://doi.org/10.1175/WAF-D-11-00151.1>, 2012.
- Cooney, J. W., Bedka, K. M., Bowman, K. P., Khlopenkov, K. V., and Iterly, K.: Comparing Tropopause-Penetrating Convection Identifications Derived from NEXRAD and GOES over the Contiguous United States, *J. Geophys. Res.-Atmos.*, 126, e2020JD034319, <https://doi.org/10.1029/2020JD034319>, 2021.
- Copernicus: Climate Data Store, <https://cds.climate.copernicus.eu/#/search?text=ERA5&type=dataset>, last access: 21 April 2023.
- de Coning, E., Gijben, M., Maseko, B., and van Hemert, L.: Using satellite data to identify and track intense thunderstorms in South and southern Africa, *S. Afr. J. Sci.*, 111, 1–5, <https://doi.org/10.17159/sajs.2015/20140402>, 2015.
- Dessens, J., Berthet, C., and Sanchez, J. L.: Change in hailstone size distributions with an increase in the melting level height, *Atmos. Res.*, 158–159, 245–253, <https://doi.org/10.1016/j.atmosres.2014.07.004>, 2015.
- Dotzek, N., Groenemeijer, P., Feuerstein, B., and Holzer, A. M.: Overview of ESSL's severe convective storms research using the European Severe Weather Database ESWD, *Atmos. Res.*, 93, 575–586, <https://doi.org/10.1016/j.atmosres.2008.10.020>, 2009.
- Dowdy, A. J., Soderholm, J., Brook, J., Brown, A., and McGowan, H.: Quantifying hail and lightning risk factors using long-term observations around Australia, *J. Geophys. Res.-Atmos.*, 125, e2020JD033101-T, <https://doi.org/10.1029/2020JD033101>, 2020.
- Dyson, L. L., Pienaar, N., Smit, A., and Kijko, A.: An ERA-Interim HAILCAST hail climatology for southern Africa, *Int. J. Climatol.*, 41, 262–277, <https://doi.org/10.1002/joc.6619>, 2020.
- Eccel, E., Cau, P., Riemann-Campe, K., and Biasioli, F.: Quantitative hail monitoring in an alpine area: 35-year climatology and links with atmospheric variables, *Int. J. Climatol.*, 32, 503–517, 2012.
- ESWD: European Severe Weather Database, <https://eswd.eu/>, last access: 21 April 2023.
- EUMETSAT: EUMETSAT Data Centre, <https://www.eumetsat.int/eumetsat-data-centre>, last access: 21 April 2023.
- Farr, T. G., Rosen, P. A., Caro, E., Crippen, R., Duren, R., Hensley, S., Kobrick, M., Paller, M., Rodriguez, E., Roth, L., Seal, D., Shaffer, S., Shimada, J., Umland, J., Werner, M., Oskin, M., Burbank, D., and Alsdorf, D.: The shuttle radar topography mission, *Rev. Geophys.*, 45, RG2004, <https://doi.org/10.1029/2005RG000183>, 2007.
- Feng, Z., Leung, L. R., Liu, N., Wang, J., Houze Jr., R. A., Li, J., Hardin, J. C., Chen, D., and Guo, J.: A Global High-Resolution Mesoscale Convective System Database Using Satellite-Derived Cloud Tops, Surface Precipitation, and Tracking, *J. Geophys. Res.-Atmos.*, 126, e2020JD034202, <https://doi.org/10.1029/2020JD034202>, 2021.
- Fluck, E., Kunz, M., Geissbuehler, P., and Ritz, S. P.: Radar-based assessment of hail frequency in Europe, *Nat. Hazards Earth Syst. Sci.*, 21, 683–701, <https://doi.org/10.5194/nhess-21-683-2021>, 2021.
- Garstang, M., Kelbe, B. E., Emmitt, G. D., and London, W. B.: Generation of Convective Storms over the Escarpment of Northeastern South Africa, *Mon. Weather Rev.*, 115, 429–443, [https://doi.org/10.1175/1520-0493\(1987\)115<0429:GOCSOT>2.0.CO;2](https://doi.org/10.1175/1520-0493(1987)115<0429:GOCSOT>2.0.CO;2), 1987.
- Gaiotti, D., Nordio, S., and Stel, F.: The climatology of hail in the plain of Friuli Venezia Giulia, *Atmos. Res.*, 67–68, 247–259, [https://doi.org/10.1016/S0169-8095\(03\)00084-X](https://doi.org/10.1016/S0169-8095(03)00084-X), 2003.
- Grieser, J. and Hill, M.: How to Express Hail Intensity-Modeling the Hailstone Size Distribution, *J. Appl. Meteorol. Clim.*, 58, 2329–2345, <https://doi.org/10.1175/JAMC-D-18-0334.1>, 2019.
- Heikenfeld, M., Marinescu, P. J., Christensen, M., Watson-Parris, D., Senf, F., van den Heever, S. C., and Stier, P.: tobac 1.2: towards a flexible framework for tracking and analysis of clouds in diverse datasets, *Geosci. Model Dev.*, 12, 4551–4570, <https://doi.org/10.5194/gmd-12-4551-2019>, 2019.
- Held, G.: Hail frequency in the Pretoria–Witwatersrand area during 1962 to 1972, *Pure Appl. Geophys.*, 112, 765–776, <https://doi.org/10.1007/BF00876951>, 1974.

- Hersbach, H., Bell, B., Berrisford, P., Hirahara, S., Horányi, A., Muñoz-Sabater, J., Nicolas, J., Peubey, C., Radu, R., Schepers, D., Simmons, A., Soci, C., Abdalla, S., Abellan, X., Balsamo, G., Bechtold, P., Biavati, G., Bidlot, J., Bonavita, M., De Chiara, G., Dahlgren, P., Dee, D., Diamantakis, M., Dragani, R., Flemming, J., Forbes, R., Fuentes, M., Geer, A., Haimberger, L., Healy, S., Hogan, R. J., Hólm, E., Janisková, M., Keeley, S., Laloyaux, P., Lopez, P., Lupu, C., Radnoti, G., de Rosnay, P., Rozum, I., Vamborg, F., Villaume, S., and Thépaut, J.-N.: The ERA5 global reanalysis, *Q. J. Roy. Meteorol. Soc.*, 146, 1999–2049, <https://doi.org/10.1002/qj.3803>, 2020.
- Junghänel, T., Brendel, C., Winterrath, T., and Walter, A.: Towards a radar- and observation-based hail climatology for Germany, *Meteorol. Z.*, 25, 435–445, <https://doi.org/10.1127/metz/2016/0734>, 2016.
- Khlopenkov, K. V., Bedka, K. M., Cooney, J. W., and Itterly, K.: Recent Advances in Detection of Overshooting Cloud Tops from Longwave Infrared Satellite Imagery, *J. Geophys. Res.-Atmos.*, 126, e2020JD034359, <https://doi.org/10.1029/2020jd034359>, 2021.
- Kunz, M., Blahak, U., Handwerker, J., Schmidberger, M., Punge, H. J., Mohr, S., Fluck, E., and Bedka, K. M.: The severe hailstorm in southwest Germany on 28 July 2013: Characteristics, impacts and meteorological conditions, *Q. J. Roy. Meteorol. Soc.*, 144, 231–250, <https://doi.org/10.1002/qj.3197>, 2018.
- Kunz, M., Wandel, J., Fluck, E., Baumstark, S., Mohr, S., and Schemm, S.: Ambient conditions prevailing during hail events in central Europe, *Nat. Hazards Earth Syst. Sci.*, 20, 1867–1887, <https://doi.org/10.5194/nhess-20-1867-2020>, 2020.
- Leigh, R. and Kuhnel, I.: Hailstorm loss modelling and risk assessment in the Sydney region, Australia, *Nat. Hazards*, 24, 171–185, <https://doi.org/10.1023/A:1011855801345>, 2001.
- Lin, Y. and Kumjian, M. R.: Influences of CAPE on hail production in simulated supercell storms, *J. Atmos. Sci.*, 79, 179–204, <https://doi.org/10.1175/JAS-D-21-0054.1>, 2022.
- Loftus, A., Cotton, W., and Carrió, G.: A triple-moment hail bulk microphysics scheme. Part I: Description and initial evaluation, *Atmos. Res.*, 149, 35–57, <https://doi.org/10.1016/j.atmosres.2014.05.013>, 2014.
- Mardia, K. V. and Zemroch, P. J.: Algorithm AS 86: The Von Mises Distribution Function, *J. Roy. Stat. Soc. C.*, 24, 268–272, <https://doi.org/10.2307/2346578>, 1975.
- Marion, G. R., Trapp, R. J., and Nesbitt, S. W.: Using Overshooting Top Area to Discriminate Potential for Large, Intense Tornadoes, *Geophys. Res. Lett.*, 46, 12520–12526, <https://doi.org/10.1029/2019GL084099>, 2019.
- Markowski, P. and Richardson, Y.: Mesoscale meteorology in midlatitudes, Wiley, Blackwell, ISBN 9780470742136, <https://doi.org/10.1002/9780470682104>, 2010.
- Melcón, P., Merino, A., Sánchez, J. L., López, L., and Hermida, L.: Satellite remote sensing of hailstorms in France, *Atmos. Res.*, 182, 221–231, <https://doi.org/10.1016/j.atmosres.2016.08.001>, 2016.
- Mohr, S., Wandel, J., Lenggenhager, S., and Martius, O.: Relationship between atmospheric blocking and warm-season thunderstorms over western and central Europe, *Q. J. Roy. Meteorol. Soc.*, 145, 3040–3056, <https://doi.org/10.1002/qj.3603>, 2019.
- Mohr, S., Wilhelm, J., Wandel, J., Kunz, M., Portmann, R., Punge, H. J., Schmidberger, M., Quinting, J. F., and Grams, C. M.: The role of large-scale dynamics in an exceptional sequence of severe thunderstorms in Europe May–June 2018, *Weather Clim. Dynam.*, 1, 325–348, <https://doi.org/10.5194/wcd-1-325-2020>, 2020.
- Mroz, K., Battaglia, A., Lang, T. J., Cecil, D. J., Tanelli, S., and Tridon, F.: Hail-Detection Algorithm for the GPM Core Observatory Satellite Sensors, *J. Appl. Meteorol. Clim.*, 56, 1939–1957, <https://doi.org/10.1175/JAMC-D-16-0368.1>, 2017.
- Munich RE: Severe convective storms and hail – Icy cricket balls from above, <http://www.munichre.com/australia/australia-natural-hazards/australia-storm/hailstorm/index.html>, last access: 25 November 2015.
- Murillo, E. M. and Homeyer, C. R.: Severe hail fall and hailstorm detection using remote sensing observations, *J. Appl. Meteorol. Clim.*, 58, 947–970, <https://doi.org/10.1175/JAMC-D-18-0247.1>, 2019.
- Murillo, E. M., Homeyer, C. R., and Allen, J. T.: A 23-Year Severe Hail Climatology Using GridRad MESH Observations, *Mon. Weather Rev.*, 149, 945–958, <https://doi.org/10.1175/MWR-D-20-0178.1>, 2021.
- Ni, X., Liu, C., Cecil, D. J., and Zhang, Q.: On the Detection of Hail Using Satellite Passive Microwave Radiometers and Precipitation Radar, *J. Appl. Meteorol. Clim.*, 56, 2693–2709, <https://doi.org/10.1175/JAMC-D-17-0065.1>, 2017.
- Nisi, L., Hering, A., Germann, U., and Martius, O.: A 15-year hail streak climatology for the Alpine region, *Q. J. Roy. Meteorol. Soc.*, 144, 1429–1449, <https://doi.org/10.1002/qj.3286>, 2018.
- NOAA: Comprehensive Large Array-Data Stewardship System (CLASS), <https://www.avl.class.noaa.gov/saa/products/welcome.jsessionid=BDF491314248B818A20B53DFF3EC97B5>, last access: 21 April 2023.
- Olivier, J.: Hail in the Transvaal – some geographical and climatological aspects, PhD thesis, Rand Afrikaans University, <https://ujcontent.uj.ac.za/esploro/outputs/graduate/Hail-in-the-Transvaal--some/9912217207691#file-0> (last access: 21 April 2023), 1990.
- Palencia, C., Castro, A., Giaiotti, D., Stel, F., Vinet, F., and Fraile, R.: Hailpad-based research: A bibliometric review, *Atmos. Res.*, 93, 664–670, 2009.
- Perry, A.: Severe hailstorm at Grahamstown in relation to convective weather hazards in South Africa, *Weather*, 50, 211–214, <https://doi.org/10.1002/j.1477-8696.1995.tb06110.x>, 1995.
- Petty, G. W. and Bennartz, R.: Field-of-view characteristics and resolution matching for the Global Precipitation Measurement (GPM) Microwave Imager (GMI), *Atmos. Meas. Tech.*, 10, 745–758, <https://doi.org/10.5194/amt-10-745-2017>, 2017.
- Powell, C. L. and Burger, R. P.: The severe Gauteng hailstorms of 28 November 2013, in: Proc. 30th Ann. Conf. South African Soc. Atmos. Sci., 1–2 October 2014, Potchefstroom, South Africa, 54–57, <http://hdl.handle.net/10394/16144> (last access: 21 April 2023), 2014.
- Prein, A. F. and Holland, G. J.: Global estimates of damaging hail hazard, *Weather Clim. Ext.*, 22, 10–23, <https://doi.org/10.1016/j.wace.2018.10.004>, 2018.
- Punge, H. and Kunz, M.: Hail observations and hailstorm characteristics in Europe: A review, *Atmos. Res.*, 176, 159–184, <https://doi.org/10.1016/j.atmosres.2016.02.012>, 2016.

- Punge, H., Bedka, K., Kunz, M., and Reinbold, A.: Hail frequency estimation across Europe based on a combination of overshooting top detections and the ERA-INTERIM reanalysis, *Atmos. Res.*, 198, 34–43, <https://doi.org/10.1016/j.atmosres.2017.07.025>, 2017.
- Punge, H. J., Bedka, K. M., Kunz, M., and Werner, A.: A new physically based stochastic event catalog for hail in Europe, *Nat. Hazards*, 73, 1625–1645, <https://doi.org/10.1007/s11069-014-1161-0>, 2014.
- Punge, H. J., Bedka, K. M., Kunz, M., and Reinbold, A.: Hail frequency estimation across Europe based on a combination of overshooting top detections and the ERA-INTERIM reanalysis, *Atmos. Res.*, 198, 34–43, <https://doi.org/10.1016/j.atmosres.2017.07.025>, 2017.
- Pučík, T., Castellano, C., Groenemeijer, P., Kühne, T., Rädler, A. T., Antonescu, B., and Faust, E.: Large Hail Incidence and Its Economic and Societal Impacts across Europe, *Mon. Weather Rev.*, 147, 3901–3916, <https://doi.org/10.1175/MWR-D-19-0204.1>, 2019.
- Puskeiler, M., Kunz, M., and Schmidberger, M.: Hail statistics for Germany derived from single-polarization radar data, *Atmos. Res.*, 178–179, 459–470, <https://doi.org/10.1016/j.atmosres.2016.04.014>, 2016.
- Rädler, A. T., Groenemeijer, P., Faust, E., and Sausen, R.: Detecting severe weather trends using an Additive Regressive Convective Hazard Model (AR-CHaMo), *J. Appl. Meteorol. Clim.*, 57, 569–587, <https://doi.org/10.1175/JAMC-D-17-0132.1>, 2018.
- Reges, H. W., Doesken, N., Turner, J., Newman, N., Bergantino, A., and Schwalbe, Z.: CoCoRaHS: The evolution and accomplishments of a volunteer rain gauge network, *B. Am. Meteorol. Soc.*, 97, 1831–1846, <https://doi.org/10.1175/BAMS-D-14-00213.1>, 2016.
- Sánchez, J., Gil-Robles, B., Dessens, J., Martin, E., Lopez, L., Marcos, J., Berthet, C., Fernández, J., and García-Ortega, E.: Characterization of hailstone size spectra in hailpad networks in France, Spain, and Argentina, *Atmos. Res.*, 93, 641–654, <https://doi.org/10.1016/j.atmosres.2008.09.033>, 2009.
- Sandmæl, T. N., Homeyer, C. R., Bedka, K. M., Apke, J. M., Mecikalski, J. R., and Khlopenkov, K.: Evaluating the Ability of Remote Sensing Observations to Identify Significantly Severe and Potentially Tornadoic Storms, *J. Appl. Meteorol. Clim.*, 58, 2569–2590, <https://doi.org/10.1175/JAMC-D-18-0241.1>, 2019.
- Scarino, B. R., Bedka, K., Bhatt, R., Khlopenkov, K., Doelling, D. R., and Smith Jr., W. L.: A kernel-driven BRDF model to inform satellite-derived visible anvil cloud detection, *Atmos. Meas. Tech.*, 13, 5491–5511, <https://doi.org/10.5194/amt-13-5491-2020>, 2020.
- Schmetz, J., Pili, P., Tjemkes, S., Just, D., Kerkmann, J., Rota, S., and Ratier, A.: An introduction to Meteosat second generation (MSG), *B. Am. Meteorol. Soc.*, 83, 977–992, [https://doi.org/10.1175/1520-0477\(2002\)083<0977:AITMSG>2.3.CO;2](https://doi.org/10.1175/1520-0477(2002)083<0977:AITMSG>2.3.CO;2), 2002.
- Schmidberger, M.: Hagelgefährdung und Hagelrisiko in Deutschland basierend auf einer Kombination von Radardaten und Versicherungsdaten, PhD thesis, Institute of Meteorology and Climate Research, KIT – Karlsruhe Institute of Technology, 263 pp., <https://publikationen.bibliothek.kit.edu/1000086012> (last access: 21 April 2023), 2018.
- Seifert, A. and Beheng, K. D.: A two-moment cloud microphysics parameterization for mixed-phase clouds. Part 1: Model description, *Meteorol. Atmos. Phys.*, 92, 45–66, <https://doi.org/10.1007/s00703-005-0112-4>, 2006.
- Sioutas, M., Meaden, T., and Webb, J. D.: Hail frequency, distribution and intensity in Northern Greece, *Atmos. Res.*, 93, 526–533, <https://doi.org/10.1016/j.atmosres.2008.09.023>, 2009.
- Smith, H., Wingfield, M., and Coutinho, T.: The role of latent Sphaeropsis sapinea infections in post-hail associated dieback of *Pinus patula*, *Forest Ecol. Manage.*, 164, 177–184, [https://doi.org/10.1016/S0378-1127\(01\)00610-7](https://doi.org/10.1016/S0378-1127(01)00610-7), 2002.
- Smith, S. B., Reuter, G. W., and Yau, M.: The episodic occurrence of hail in central Alberta and the Highveld of South Africa: Research note, *Atmos.-Ocean*, 36, 169–178, <https://doi.org/10.1080/07055900.1998.9649610>, 1998.
- Stout, G., Blackmer, R., and Wilk, K.: Hail studies in Illinois relating to cloud physics, *Physics of Precipitation, Geophys. Monogr.*, 5, 369–381, <https://doi.org/10.1029/GM005p0369>, 1960.
- Taszarek, M., Allen, J., Pučík, T., Groenemeijer, P., Czernecki, B., Kolendowicz, L., Lagouvardos, K., Kotroni, V., and Schulz, W.: A climatology of thunderstorms across Europe from a synthesis of multiple data sources, *J. Climate*, 32, 1813–1837, <https://doi.org/10.1175/JCLI-D-18-0372.1>, 2019.
- Taszarek, M., Allen, J. T., Pučík, T., Hoogewind, K. A., and Brooks, H. E.: Severe convective storms across Europe and the United States. Part 2: ERA5 environments associated with lightning large hail, severe wind and tornadoes, *J. Climate*, 33, 10263–10286, <https://doi.org/10.1175/JCLI-D-20-0346.1>, 2020.
- University of Oklahoma: 3-D Gridded NEXRAD WSR-88D Radar Data, <http://gridrad.org/data.html>, last access: 21 April 2023.
- Wellmann, C., Barrett, A. I., Johnson, J. S., Kunz, M., Vogel, B., Carslaw, K. S., and Hoose, C.: Comparing the impact of environmental conditions and microphysics on the forecast uncertainty of deep convective clouds and hail, *Atmos. Chem. Phys.*, 20, 2201–2219, <https://doi.org/10.5194/acp-20-2201-2020>, 2020.
- Wilhelm, J., Mohr, S., Punge, H. J., Mühr, B., Schmidberger, M., Daniell, J. E., Bedka, K. M., and Kunz, M.: Severe thunderstorms with large hail across Germany in June 2019, *Weather*, 76, 228–237, <https://doi.org/10.1002/wea.3886>, 2021.
- Wilks, D. S.: *Statistical Methods in the Atmospheric Sciences: An Introduction*, Academic Press, ISBN 9780080541723, 1995.
- Wingfield, M. J. and Swart, W. J.: Integrated management of forest tree diseases in South Africa, *Forest Ecol. Manage.*, 65, 11–16, [https://doi.org/10.1016/0378-1127\(94\)90253-4](https://doi.org/10.1016/0378-1127(94)90253-4), 1994.
- Zinner, T., Forster, C., de Coning, E., and Betz, H.-D.: Validation of the Meteosat storm detection and nowcasting system Cb-TRAM with lightning network data – Europe and South Africa, *Atmos. Meas. Tech.*, 6, 1567–1583, <https://doi.org/10.5194/amt-6-1567-2013>, 2013.